Three-dimensional thermal stress analysis of multilayered piezoelectric curved panels

Composite Structures 387 (2026) 120338

Contents lists available at ScienceDirect

Composite Structures

journal homepage: www.elsevier.com/locate/compstruct

Three-dimensional thermal stress analysis of multilayered piezoelectric curved panels

S. Brischetto *, D. Cesare, T. Mondino

Department of Mechanical and Aerospace Engineering, Politecnico di Torino, Torino, Italy

ARTICLE INFO

The first author dedicates this work to the memory of his beloved father and his dear uncle.

Keywords:
Three-dimensional model
Analytical solution
Thermal stress analysis
Piezoelectric shell structures
Layer-wise approach
Exponential matrix method
Thermo-electro-elastic coupling

ABSTRACT

In the present work, the thermal stress analysis of curved multilayered piezoelectric structures is presented. The proposed analytical formulation directly models, in a three-dimensional (3D) form, displacements, electric potential, and temperature. The 3D equilibrium equations, the 3D divergence equation for the electric displacement, and the 3D Fourier heat conduction equation constitute the 3D governing equations for the thermal stress analysis of spherical shells involving the thermo-electro-elastic (TEE) coupling. The 3D governing equations are written for spherical shells via an orthogonal mixed curvilinear reference system (α, β, z). Degeneration into cylindrical panels, cylinders, and plates is possible by properly considering appropriate values for radii of curvature R_α and R_β. Navier harmonic forms in the two in-plane directions and the exponential matrix method in the thickness direction are adopted, and simply-supported constraints are imposed. Several load boundary conditions can be considered in terms of temperature, electric potential, pressure load, and heat flux at the outer surfaces. The adopted layer-wise approach considers the interlaminar continuity conditions of elastic displacement, electric potential, temperature, transverse shear and transverse normal stresses, transverse normal electric displacement, and transverse normal heat flux. In the validation cases subsection, the present 3D model is compared with other 3D analytical models for piezoelectric multilayered structures. In the new cases subsection, several geometries and load boundary conditions are proposed for different thickness ratios and lamination schemes. Therefore, TEE coupling, material layer, thickness layer and curvature effects, are clearly shown in tabular and graphical forms. The main novelty is that the equations are general, as they are applicable to different geometries, such as plates, cylindrical shells, and spherical shells, allowing the study of the full coupling among elastic, thermal, and electrical fields without increasing computational costs, despite a 3D, layer-wise approach.

1. Introduction

Curved and flat panels are widely used in the aeronautical and aerospace sectors because of their well-known capacity to withstand operational flight loads. In the last four decades, multilayered spherical shells have made significant advances in the design of aerospace structures because of the effects of curvature on load-bearing capability [1–3]. In recent years, new challenges have had to be addresses by aerostructure designers to improve flight comfort for passengers and to make flights more efficient in terms of fuel consumption in response to increasing environmental requirements. In this framework, thermal stress analysis of multilayered piezoelectric spherical shells is a crucial aspect in desing aerostructures able to withstand operational flight loads.

Researchers and scientists working in the field of innovative structures for aerospace purposes are highly interested in the thermal stress analysis of piezoelectric structures, and have developed both numerical and analytical models [4–6] from a two-dimensional (2D) or three-dimensional (3D) point of view. In the present study, the thermal stress analysis of multilayered piezoelectric spherical shells accounting for thermo-electro-elastic (TEE) coupling is investigated. The orthogonal mixed curvilinear reference system allows the degeneration of the spherical shell geometry into simpler geometries (cylinders, cylindrical panels and plates), while properly accounting for the radii of curvature. Navier harmonic forms in the in-plane directions and the exponential matrix method in the thickness direction are adopted. In this manner, all the 3D effects involved in TEE curved structures (material layer, thickness layer, TEE coupling, and curvature effects) are accurately captured.

Exact 3D/2D models have not any numerical problems and errors and for these reasons they are very useful tools to validate numerical

* Correspondence to: Department of Mechanical and Aerospace Engineering, Politecnico di Torino, corso Duca degli Abruzzi 24, 10129 Torino, Italy.
E-mail address: salvatore.brischetto@polito.it (S. Brischetto).

https://doi.org/10.1016/j.compstruct.2026.120338
Received 3 February 2026; Received in revised form 17 March 2026; Accepted 6 April 2026
Available online 6 April 2026

models. The transient response of simply-supported functionally graded plates embedding piezoelectric layers under electric field loads and thermal shock was analyzed by Alibeigloo [7]. The TEE transient response for piezoelectric hollow structures subjected to thermal shocks, sudden mechanical loads and electric excitation was investigated in [8]. Dube et al. [9] proposed an exact piezothermoelastic model for infinitely long simply-supported orthotropic plates under different mechanical, thermal and electrostatic loads. Georgiades et al. [10] showed different asymptotic homogenization models for prismatic smart composite structures including elastic, piezoelectric, and thermal expansion coefficients. Kapuria et al. [11,12] presented a 3D axisymmetric solution for a simply supported piezoelectric and cross-ply cylindrical shell under axisymmetric thermoelectromechanical loads. In the framework of the method of sampling surfaces, the exact 3D TEE solutions of the steady-state problem for piezoelectric laminated plates and shells subjected to thermal loading were developed by Kulikov et al. [13,14]. A 3D TEE static problem solution for 3D transversely isotropic bodies was proposed in [15]. An analytical approach for the nonlinear forced vibration of imperfect pentagraphene plates integrated with piezoelectric actuator layers was proposed by Quoc Quan et al. in [16]. Tang et al. [17] presented a static TEE response of multilayered hybrid composite plates considering different 2D approaches. In the work proposed by Tauchert [18], the cylindrical bending of a composite plate made of orthotropic thermoelastic layers and orthorhombic piezoelectric layers was analyzed considering a high-order plane strain analysis for transverse normal and shear deformations. Xu et al. [19] developed a 3D solution for the coupled TEE response of multilayered hybrid composite piezothermoelastic plates. Zhang et al. [20,21] proposed an eigenvalue model and coupled piezoelectric differential equations for composite laminated plates with piezoelectric layers and piezo-thermoelastic layers under cylindrical bending. Von Karman nonlinearity and classical thin shell theory were adopted in the free vibration analysis by Gia Ninh and Duc Tien [22] to investigate conveying-fluid functionally graded carbon nanotube reinforced composite cylindrical shells with piezoelectric layers in thermal environment. The steady-state solutions were presented in [23] for the coupled TEE forced vibrations of piezoelectric laminated beams considering different types of damping.

Scientists and researchers use numerical methods to analyze real aerostructures with more complicated geometries and boundary conditions. Ahmad et al. [24] proposed a coupled layer-by-layer Finite Element (FE) TEE model to analyze the capabilities of structures embedding piezoelectric patches. A model for the static TEE problem with friction was presented in [25]. Chen et al. [26] showed a zero-order multiphysics finite-volume micromechanics model for the TEE coupling of unidirectional composites embedding piezoelectric phases. In Cho and Oh [27], a high-order zig-zag plate theory was developed to couple mechanical, thermal and electric fields. Primary degrees of freedom for displacements and temperature were layer-dependent. Jian and Li [28] presented a FE model for the mechanical, electrical and thermal response of piezoelectric composite plates considering a high-order displacement field, a quadratic electric potential field and a linear temperature field. In Li et al. [29], the 3D TEE static solution was presented in terms of five quasi-harmonic functions for an infinite/half-infinite space of one-dimensional hexagonal quasi-crystals. In [30], a set of axisymmetric solutions was shown for a circular plate including functionally graded materials and loaded with the temperature field applied on the two outer surfaces. Liew et al. [31] investigated the behavior of multilayered composite plates subjected to thermo-piezoelectric-mechanical loadings; 3D equations for thermo-piezoelasticity were solved using the differential quadrature method. A laminated plate model adopting the variational asymptotic method was developed by Long and Yu [32]. In Moradi-Dastjerdi and Behdinan [33], a meshless method was developed for the analysis of stresses and deflections of advanced smart lightweight sandwich plates subjected to TEE loads. Tornabene et al. [34] introduced a refined formulation for the TEE analysis of smart laminated shells using a generalized differential quadrature model. The Lord–Shulman TEE theory and the nonlocal integral elasticity effect were employed by Wang et al. [35] to investigate the plane wave propagation in sandwiched functionally graded nanoplates. Wu et al. [36] developed a meshless collocation method for the 3D coupled analysis of simply-supported, doubly curved functionally graded TEE shells based on the differential reproducing kernel interpolation. The Reissner–Mindlin model for laminated composite plates including piezoelectric layers under mechanical, thermal and electric loads was constructed by Yu and Hodges [37] using the variational-asymptotic method. The same authors extended the previous work to TEE smart composite shells in [38]. Zenkour and Alghanmi [39] presented an analysis of the static bending of a sandwich plate resting on Pasternak's elastic foundations composed of a functionally graded core and piezoelectric face sheets.

This work tries to fill a gap in the aerospace structures field related to the 3D thermal stress analysis of multilayered piezoelectric shells. The main novelty is the full coupling between thermal, electric, and elastic fields using 3D governing equations for the TEE spherical shell problem, which can degenerate into those for simpler geometries, such as cylindrical panels and plates. The full TEE coupling is possible thanks to the use of 3D equilibrium equations, the 3D divergence equation for the electric displacement, and the 3D Fourier heat conduction equation. This set of five 3D equations for spherical shells (written in an orthogonal mixed curvilinear reference system) is solved analytically in closed-form. The closed-form solution consists of employing Navier harmonic forms in the in-plane directions and the exponential matrix method in the thickness direction. The use of the mixed curvilinear reference system allows the analysis of four different geometries using a unique set of 3D equations. By imposing appropriate radius of curvature values, degeneration into plate, cylindrical panel, and cylinder geometries is possible. The present methodology is very powerful because stresses, strains, electric displacements and heat fluxes are computed exactly. In fact, first derivatives with respect to z of the independent variables are exactly computed within the exponential matrix method because they are primary unknowns of the proposed model. In addition, the layer-wise approach is implemented through interlaminar continuity conditions for displacements, temperature, electric potential, transverse shear/normal stresses, transverse normal electric displacement and transverse normal heat flux. The present paper is the extension of the following works: the static elastic study of multilayered and sandwich structures in [40], the static electro-elastic study of structures involving piezoelectric layers in [41] and the thermal stress analysis of multilayered structures in [42].

The present paper is organized as follows: Section 2 presents the 3D equations for the thermal stress analysis of piezoelectric structures, while Section 3 presents the results. Section 3 considers a validation subsection and another subsection dedicated to new benchmarks. Section 4 presents the main conclusions.

2. 3D governing, geometrical and constitutive equations for the thermal stress analysis of piezoelectric spherical panels

The 3D exact thermo-electro-elastic model for spherical shells is proposed in this section. 3D constitutive equations and geometric relations are presented for spherical shells. Then, the 3D equilibrium equations, the 3D divergence equation for the electric displacement and the 3D Fourier heat conduction equation, written in an orthogonal mixed curvilinear reference system are proposed. Finally, the exponential matrix methodology is given in detail for the thermo-electro-elastic analysis. The four investigated geometries are shown in Fig. 1, where the orthogonal mixed curvilinear reference system (α, β, z) for each geometry and the middle reference surface Ω_0 are defined. In-plane directions α and β follow the curvature of the geometry, and the z direction is rectilinear and perpendicular to the middle reference surface Ω_0.

2.1. Constitutive and geometrical relations

Constitutive relations for the 3D thermal stress analysis of spherical panels embedding piezoelectric layers allow the coupling between thermal, electric and elastic fields:

$$\boldsymbol{\sigma}^k = \boldsymbol{C}^k \boldsymbol{\epsilon}^k - \boldsymbol{e}^{kT} \boldsymbol{\mathcal{E}}^k - \boldsymbol{\lambda}^k \theta^k, \tag{1}$$

$$\boldsymbol{D}^k = \boldsymbol{e}^k \boldsymbol{\epsilon}^k + \boldsymbol{\epsilon}^k \boldsymbol{\mathcal{E}}^k - \boldsymbol{p}^k \theta^k, \tag{2}$$

$$\boldsymbol{q}^k = -\boldsymbol{k}^k \boldsymbol{\nabla} \theta^k, \tag{3}$$

where $\boldsymbol{\sigma}^k = \{\sigma^k_{\alpha\alpha}\ \sigma^k_{\beta\beta}\ \sigma^k_{zz}\ \sigma^k_{\beta z}\ \sigma^k_{\alpha z}\ \sigma^k_{\alpha\beta}\}^T$ is the 6×1 stress vector, $\boldsymbol{\epsilon}^k = \{\epsilon^k_{\alpha\alpha}\ \epsilon^k_{\beta\beta}\ \epsilon^k_{zz}\ \gamma^k_{\beta z}\ \gamma^k_{\alpha z}\ \gamma^k_{\alpha\beta}\}^T$ is the 6×1 strain vector, $\boldsymbol{\mathcal{E}}^k = \{\mathcal{E}^k_\alpha\ \mathcal{E}^k_\beta\ \mathcal{E}^k_z\}^T$ is the 3×1 electric field vector, $\theta^k = T - T_0$ is the scalar over-temperature (where T is the applied temperature and T_0 is the reference room temperature), $\boldsymbol{\mathcal{D}}^k = \{\mathcal{D}^k_\alpha\ \mathcal{D}^k_\beta\ \mathcal{D}^k_z\}^T$ is the 3×1 electric displacement vector, $\boldsymbol{q}^k = \{q^k_\alpha\ q^k_\beta\ q^k_z\}^T$ is the 3×1 heat flux vector. k and T superscripts specify a generic physical layer of the multilayered structure and the transpose of a matrix/vector, respectively.

The 6×6 elastic coefficients matrix in the structural reference system is:

$$\boldsymbol{C}^k = \begin{bmatrix} C^k_{11} & C^k_{12} & C^k_{13} & 0 & 0 & C^k_{16} \\ C^k_{12} & C^k_{22} & C^k_{23} & 0 & 0 & C^k_{26} \\ C^k_{13} & C^k_{23} & C^k_{33} & 0 & 0 & C^k_{36} \\ 0 & 0 & 0 & C^k_{44} & C^k_{45} & 0 \\ 0 & 0 & 0 & C^k_{45} & C^k_{55} & 0 \\ C^k_{16} & C^k_{26} & C^k_{36} & 0 & 0 & C^k_{66} \end{bmatrix}. \tag{4}$$

The 3×6 piezoelectric coefficients matrix is:

$$\boldsymbol{e}^k = \begin{bmatrix} 0 & 0 & 0 & e^k_{14} & e^k_{15} & 0 \\ 0 & 0 & 0 & e^k_{24} & e^k_{25} & 0 \\ e^k_{31} & e^k_{32} & e^k_{33} & 0 & 0 & e^k_{36} \end{bmatrix}. \tag{5}$$

The 6×1 thermo-elastic coupling coefficients vector is the product between the 6×6 elastic coefficients matrix $\boldsymbol{C}^k$ and the 6×1 thermal expansion coefficients vector $\boldsymbol{\mu}^k$:

$$\boldsymbol{\lambda}^k = \begin{Bmatrix} \lambda^k_{11} \\ \lambda^k_{22} \\ \lambda^k_{33} \\ 0 \\ 0 \\ \lambda^k_{12} \end{Bmatrix} = \boldsymbol{C}^k \boldsymbol{\mu}^k = \boldsymbol{C}^k \begin{Bmatrix} \mu^k_{11} \\ \mu^k_{22} \\ \mu^k_{33} \\ 0 \\ 0 \\ \mu^k_{12} \end{Bmatrix}. \tag{6}$$

The 3×3 electric permittivity coefficients matrix $\boldsymbol{\epsilon}^k$ is:

$$\boldsymbol{\epsilon}^k = \begin{bmatrix} \epsilon^k_{11} & \epsilon^k_{12} & 0 \\ \epsilon^k_{12} & \epsilon^k_{22} & 0 \\ 0 & 0 & \epsilon^k_{33} \end{bmatrix}. \tag{7}$$

The 3×1 pyroelectric coefficients vector $\boldsymbol{p}^k$ is:

$$\boldsymbol{p}^k = \begin{Bmatrix} 0 \\ 0 \\ p^k_3 \end{Bmatrix}. \tag{8}$$

The 3×3 heat conduction coefficients matrix $\boldsymbol{k}^k$ is:

$$\boldsymbol{k}^k = \begin{bmatrix} k^k_{11} & k^k_{12} & 0 \\ k^k_{12} & k^k_{22} & 0 \\ 0 & 0 & k^k_{33} \end{bmatrix}. \tag{9}$$

The 3×1 vector $\boldsymbol{\nabla}$ includes the spatial derivatives for α, β and z coordinates:

$$\boldsymbol{\nabla} = \begin{bmatrix} \frac{1}{H_\alpha}\frac{\partial}{\partial\alpha} \\ \frac{1}{H_\beta}\frac{\partial}{\partial\beta} \\ \frac{\partial}{\partial z} \end{bmatrix}. \tag{10}$$

Geometrical relations link the strain vector $\boldsymbol{\epsilon}^k$ and the electric field vector $\boldsymbol{\mathcal{E}}^k$ with the displacement vector $\boldsymbol{u}^k$ and the scalar electric potential ϕ^k, respectively:

$$\boldsymbol{\epsilon}^k = \boldsymbol{G}\, \boldsymbol{u}^k, \tag{11}$$

$$\boldsymbol{\mathcal{E}}^k = -\boldsymbol{\nabla}\, \phi^k, \tag{12}$$

where $\boldsymbol{G}$ is the 6×3 spherical shell derivatives matrix for the elastic field, $\boldsymbol{u}^k = \{u^k\ v^k\ w^k\}^T$ is the 3×1 displacement vector. In the mixed curvilinear reference system, the spherical shell derivatives matrix is:

$$\boldsymbol{G} = \begin{bmatrix} \frac{1}{H_\alpha}\frac{\partial}{\partial\alpha} & 0 & \frac{1}{H_\alpha R_\alpha} \\ 0 & \frac{1}{H_\beta}\frac{\partial}{\partial\beta} & \frac{1}{H_\beta R_\beta} \\ 0 & 0 & \frac{\partial}{\partial z} \\ 0 & \frac{\partial}{\partial z} - \frac{1}{H_\beta R_\beta} & \frac{1}{H_\beta}\frac{\partial}{\partial\beta} \\ \frac{\partial}{\partial z} - \frac{1}{H_\alpha R_\alpha} & 0 & \frac{1}{H_\alpha}\frac{\partial}{\partial\alpha} \\ \frac{1}{H_\beta}\frac{\partial}{\partial\beta} & \frac{1}{H_\alpha}\frac{\partial}{\partial\alpha} & 0 \end{bmatrix}, \tag{13}$$

where R_α and R_β are radii of curvature of the middle reference surface Ω_0 in α and β directions, respectively. Parametric coefficients H_α and H_β are defined as follows:

$$H_\alpha = H_\alpha(z) = 1 + \frac{z}{R_\alpha} = 1 + \frac{\tilde{z} - h/2}{R_\alpha}, \tag{14}$$

$$H_\beta = H_\beta(z) = 1 + \frac{z}{R_\beta} = 1 + \frac{\tilde{z} - h/2}{R_\beta}, \tag{15}$$

where $-h/2 < z < h/2$ and $0 < \tilde{z} < h$. z is rectilinear and related H_z equals 1. $\frac{\partial}{\partial\alpha}$, $\frac{\partial}{\partial\beta}$ and $\frac{\partial}{\partial z}$ express the partial derivatives in each direction. h is considered as the total thickness of the structure. $H_\alpha = H_\beta = 1$ for plates because $R_\alpha = R_\beta = \infty$; $H_\alpha = H_\alpha(z)$ and $H_\beta = 1$ for cylindrical panels and cylinders because $R_\alpha \neq \infty$ and $R_\beta = \infty$ (see Fig. 1).

2.2. 3D governing equations

The 3D governing equations for the thermal stress analysis of piezoelectric spherical panels consist of 3D equilibrium equations, the 3D divergence equation for the electric displacement and the 3D Fourier heat conduction equation in steady-state conditions. The complete set of equations for the spherical shell case in the orthogonal mixed curvilinear reference system is:

$$H_\beta \frac{\partial \sigma^k_{\alpha\alpha}}{\partial\alpha} + H_\alpha \frac{\partial \sigma^k_{\alpha\beta}}{\partial\beta} + H_\alpha H_\beta \frac{\partial \sigma^k_{\alpha z}}{\partial z} + \left(\frac{2H_\beta}{R_\alpha} + \frac{H_\alpha}{R_\beta}\right)\sigma^k_{\alpha z} = 0, \tag{16}$$

$$H_\beta \frac{\partial \sigma^k_{\alpha\beta}}{\partial\alpha} + H_\alpha \frac{\partial \sigma^k_{\beta\beta}}{\partial\beta} + H_\alpha H_\beta \frac{\partial \sigma^k_{\beta z}}{\partial z} + \left(\frac{2H_\alpha}{R_\beta} + \frac{H_\beta}{R_\alpha}\right)\sigma^k_{\beta z} = 0, \tag{17}$$

$$H_\beta \frac{\partial \sigma^k_{\alpha z}}{\partial\alpha} + H_\alpha \frac{\partial \sigma^k_{\beta z}}{\partial\beta} + H_\alpha H_\beta \frac{\partial \sigma^k_{zz}}{\partial z} - \frac{H_\beta}{R_\alpha}\sigma^k_{\alpha\alpha} - \frac{H_\alpha}{R_\beta}\sigma^k_{\beta\beta} + \left(\frac{H_\beta}{R_\alpha} + \frac{H_\alpha}{R_\beta}\right)\sigma^k_{zz} = 0, \tag{18}$$

$$\frac{1}{H_\alpha}\frac{\partial D^k_\alpha}{\partial\alpha} + \frac{1}{H_\beta}\frac{\partial D^k_\beta}{\partial\beta} + \frac{\partial D^k_z}{\partial z} = 0, \tag{19}$$

$$\frac{1}{H_\alpha}\frac{\partial q^k_\alpha}{\partial\alpha} + \frac{1}{H_\beta}\frac{\partial q^k_\beta}{\partial\beta} + \frac{\partial q^k_z}{\partial z} = 0. \tag{20}$$

Eqs. (16)–(18) were explicitly explained in [43], Eq. (19) was obtained in [44] using the methodology explained in Povstenko [45], Eq. (20) was proposed by Povstenko [45] in completely curved coordinates.

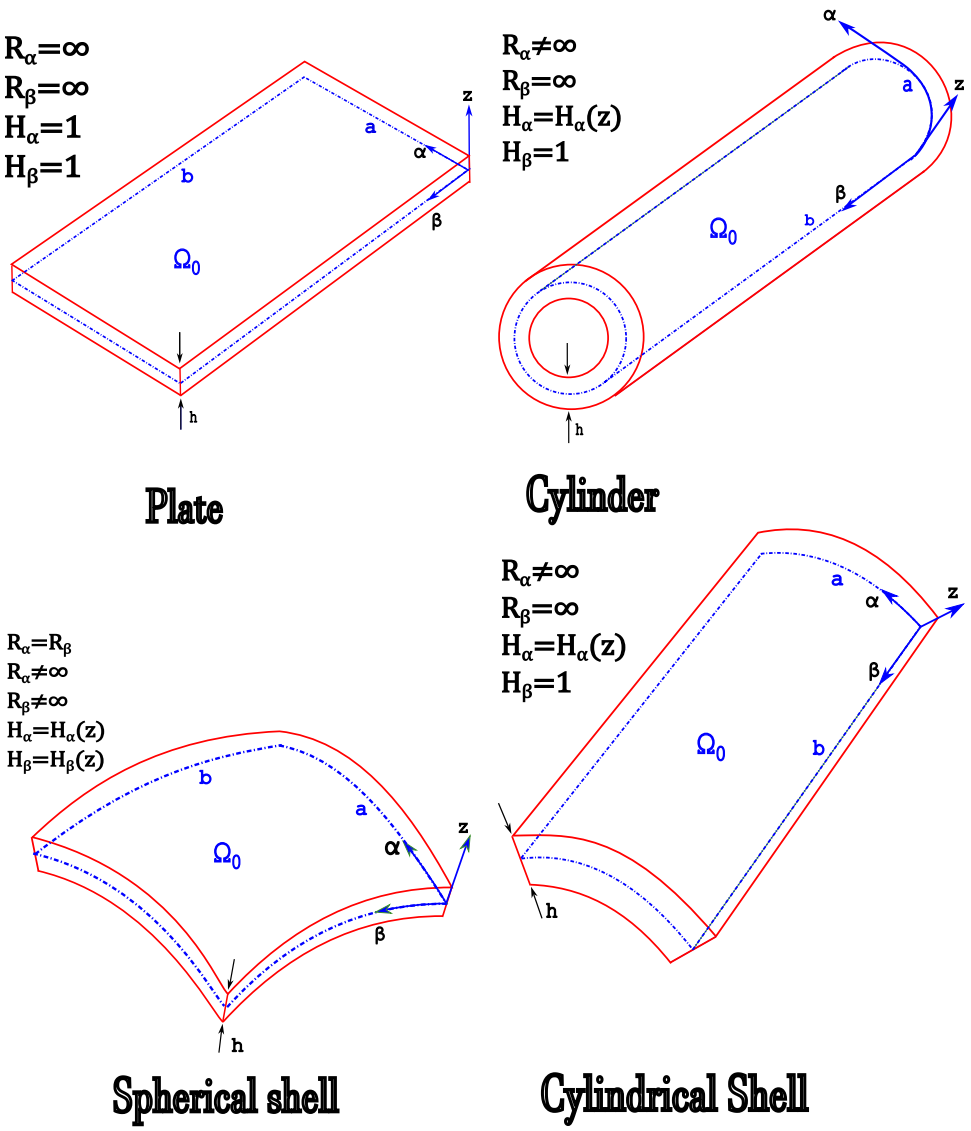

Fig. 1. Investigated geometries using the mixed curvilinear orthogonal reference system (α, β, z). Dotted lines indicate the middle reference surface Ω_0.

2.3. Exponential matrix methodology and Navier harmonic forms

Constitutive and geometrical relations (Eqs. (1)–(3), (11) and (12)) are introduced in Eqs. (16)–(20) to obtain 3D governing equations for the thermal stress analysis of piezoelectric curved panels in terms of u^k, v^k, w^k, ϕ^k and θ and related derivatives with respect to z. These five variables are called *primary variables* of the problem. A closed-form solution is possible if the following terms are set to zero:

$$C^k_{16} = C^k_{26} = C^k_{36} = C^k_{45} = 0, \quad \epsilon^k_{12} = 0, \quad \lambda^k_{12} = 0, \tag{21}$$

$$e^k_{14} = e^k_{25} = e^k_{36} = 0, \quad k^k_{12} = 0. \tag{22}$$

Eqs. (21) and (22) mean orthotropic angle equals 0° or 90°. The solution methodology for Eqs. (16)–(20) uses the Navier harmonic forms for the primary variables in the in-plane directions α and β. These harmonic forms mean simply supported sides:

$$u^k(\alpha,\beta,z) = U^k(z)\cos(\bar{\alpha}\alpha)\sin(\bar{\beta}\beta), \tag{23}$$

$$v^k(\alpha,\beta,z) = V^k(z)\sin(\bar{\alpha}\alpha)\cos(\bar{\beta}\beta), \tag{24}$$

$$w^k(\alpha,\beta,z) = W^k(z)\sin(\bar{\alpha}\alpha)\sin(\bar{\beta}\beta), \tag{25}$$

$$\phi^k(\alpha,\beta,z) = \Phi^k(z)\sin(\bar{\alpha}\alpha)\sin(\bar{\beta}\beta), \tag{26}$$

$$\theta^k(\alpha,\beta,z) = \Theta^k(z)\sin(\bar{\alpha}\alpha)\sin(\bar{\beta}\beta). \tag{27}$$

where $U^k(z)$, $V^k(z)$, $W^k(z)$, $\Phi^k(z)$ and $\Theta^k(z)$ are the maximum amplitudes of each harmonic form when both sine and cosine are equal to 1 at the same time. Terms $\bar{\alpha}$ and $\bar{\beta}$ can be written as:

$$\bar{\alpha} = \frac{m\pi}{a}, \qquad \bar{\beta} = \frac{n\pi}{b}, \tag{28}$$

where m and n are the half-wave numbers and a and b are the two in-plane dimensions.

Navier harmonic forms in Eqs. (23)–(27) automatically satisfy simply-supported boundary conditions at the edges. Simply-supported constraint conditions can be written as follows:

$$v^k = 0, \quad w^k = 0, \quad \phi^k = 0, \quad \theta^k = 0, \quad \sigma^k_{\alpha\alpha} = 0 \quad \text{for} \quad \alpha = 0, a, \tag{29}$$

$$u^k = 0, \quad w^k = 0, \quad \phi^k = 0, \quad \theta^k = 0, \quad \sigma^k_{\beta\beta} = 0 \quad \text{for} \quad \beta = 0, b. \tag{30}$$

Simply supported constraint conditions are satisfied on the edges for each k physical layer. Introducing the Navier harmonic forms of Eqs. (23)–(27) in Eqs. (16)–(20), derivatives of primary variables along α and β directions can be exactly computed as sine and cosine

derivatives are known. In this way, governing equations are functions of the z coordinate. Therefore, the new compact form is:

$$A_1^k U^k + A_2^k V^k + A_3^k W^k + A_4^k \Phi^k + J_1^k \Theta^k + A_5^k U_{,z}^k + A_6^k W_{,z}^k + A_7^k \Phi_{,z}^k + \\ + A_8^k U_{,zz}^k = 0, \tag{31}$$

$$A_9^k U^k + A_{10}^k V^k + A_{11}^k W^k + A_{12}^k \Phi^k + J_2^k \Theta^k + A_{13}^k U_{,z}^k + A_{14}^k W_{,z}^k + A_{15}^k \Phi_{,z}^k + \\ + A_{16}^k V_{,zz}^k = 0, \tag{32}$$

$$A_{17}^k U^k + A_{18}^k V^k + A_{19}^k W^k + A_{20}^k \Phi^k + J_3^k \Theta^k + A_{21}^k U_{,z}^k + A_{22}^k V_{,z}^k + A_{23}^k W_{,z}^k + \\ + A_{24}^k \Phi_{,z}^k + J_4^k \Theta_{,z}^k + A_{25}^k W_{,zz}^k + A_{26}^k \Phi_{,zz}^k = 0, \tag{33}$$

$$A_{27}^k U^k + A_{28}^k V^k + A_{29}^k W^k + A_{30}^k \Phi^k + A_{31}^k U_{,z}^k + A_{32}^k V_{,z}^k \\ + A_{33}^k W_{,z}^k + J_4^k \Theta_{,z}^k + A_{34}^k W_{,zz}^k + \\ + A_{35}^k \Phi_{,zz}^k = 0, \tag{34}$$

$$J_5^k \Theta^k + J_6^k \Theta_{,zz}^k = 0. \tag{35}$$

where A_i^k and J_i^k coefficient terms include material characteristics, half-wave numbers, geometry and curvature terms. In order to solve Eqs. (31)–(35) using the exponential matrix method, constant values of A_i^k and J_i^k are required. A_i^k and J_i^k depend on z due to the curvature terms $H_\alpha(z)$ and $H_\beta(z)$. Therefore, each k physical layer is divided into a proper number of thin mathematical layers j. In these j mathematical layers, the curvature terms H_α and H_β can be assumed as constant and evaluated in each middle surface. Therefore, terms A_i^j and J_i^j become constant. In this way, Eqs. (31)–(35) will be referred to a general j mathematical layer. No differences occur in the model as each j mathematical layer is a subdivision of a k physical layer. The total number of mathematical layers will be addressed with M. The system of second-order differential equations in terms of the primary variables must be reduced to a first-order one by doubling the number of variables. Then, the first derivatives of the five primary variable amplitudes with respect to z ($U_{,z}$, $V_{,z}$, $W_{,z}$, $\Phi_{,z}$, $\Theta_{,z}$) become additional unknowns of the problem. In matrix form, Eqs. (31)–(35) can be rewritten as:

$$\boldsymbol{D}^j \boldsymbol{X}_{,z}^j = \boldsymbol{A}^j \boldsymbol{X}^j \quad \Rightarrow \quad \left(\boldsymbol{D}^j\right)^{-1} \boldsymbol{D}^j \boldsymbol{X}_{,z}^j = \left(\boldsymbol{D}^j\right)^{-1} \boldsymbol{A}^j \boldsymbol{X}^j \quad \Rightarrow \quad \boldsymbol{X}_{,z}^j = \boldsymbol{A}^{*j} \boldsymbol{X}^j \tag{36}$$

where matrices and vectors involved in Eq. (36) are:

$$\boldsymbol{X}^j = \begin{Bmatrix} U \\ V \\ W \\ \Phi \\ \Theta \\ U_{,z} \\ V_{,z} \\ W_{,z} \\ \Phi_{,z} \\ \Theta_{,z} \end{Bmatrix}^j, \tag{37}$$

$$\boldsymbol{D}^j = \begin{bmatrix} A_8 & 0 & 0 & 0 & 0 & 0 & 0 & 0 & 0 & 0 \\ 0 & A_{16} & 0 & 0 & 0 & 0 & 0 & 0 & 0 & 0 \\ 0 & 0 & P_1 & 0 & 0 & 0 & 0 & 0 & 0 & 0 \\ 0 & 0 & 0 & P_1 & 0 & 0 & 0 & 0 & 0 & 0 \\ 0 & 0 & 0 & 0 & J_6 & 0 & 0 & 0 & 0 & 0 \\ 0 & 0 & 0 & 0 & 0 & A_8 & 0 & 0 & 0 & 0 \\ 0 & 0 & 0 & 0 & 0 & 0 & A_{16} & 0 & 0 & 0 \\ 0 & 0 & 0 & 0 & 0 & 0 & 0 & P_1 & 0 & 0 \\ 0 & 0 & 0 & 0 & 0 & 0 & 0 & 0 & P_1 & 0 \\ 0 & 0 & 0 & 0 & 0 & 0 & 0 & 0 & 0 & J_6 \end{bmatrix}^j, \tag{38}$$

$$\boldsymbol{A}^j = \begin{bmatrix} 0 & 0 & 0 & 0 & 0 & A_8 & 0 & 0 & 0 & 0 \\ 0 & 0 & 0 & 0 & 0 & 0 & A_{16} & 0 & 0 & 0 \\ 0 & 0 & 0 & 0 & 0 & 0 & 0 & P_1 & 0 & 0 \\ 0 & 0 & 0 & 0 & 0 & 0 & 0 & 0 & P_1 & 0 \\ 0 & 0 & 0 & 0 & 0 & 0 & 0 & 0 & 0 & J_6 \\ -A_1 & -A_2 & -A_3 & -A_4 & -J_1 & -A_5 & 0 & -A_6 & -A_7 & 0 \\ -A_7 & -A_8 & -A_9 & -A_{10} & -J_2 & 0 & -A_{11} & -A_{12} & -A_{13} & 0 \\ -P_2 & -P_3 & -P_4 & -P_5 & -P_6 & -P_7 & -P_8 & -P_9 & -P_{10} & -P_{11} \\ -P_{12} & -P_{13} & -P_{14} & -P_{15} & -P_{16} & -P_{17} & -P_{18} & -P_{19} & -P_{20} & -P_{21} \\ 0 & 0 & 0 & 0 & -J_5 & 0 & 0 & 0 & 0 & 0 \end{bmatrix}^j, \tag{39}$$

where P_i terms are products between A_i and J_i terms. The $\boldsymbol{X}_{,z}^j$ vector is the unknown vector derived in the z direction. The solution of Eq. (36) with the exponential matrix method can be written using the Taylor expansion by using the thickness coordinate $\tilde{z}_j$ (from 0 to h_j):

$$\boldsymbol{X}^j\left(h_j\right) = exp\left(\boldsymbol{A}^{*j} h_j\right) \boldsymbol{X}^j(0) = \left[\sum_{i=0}^{N} \frac{(\boldsymbol{A}^{*j})^i}{i!} h_j^i\right] \boldsymbol{X}^j(0) = \boldsymbol{A}^{**j} \boldsymbol{X}^j(0), \tag{40}$$

considering the exponential matrix evaluated for the thickness h_j of each j mathematical layer. For $i = 0$, $(\boldsymbol{A}^{*j})^0 = \boldsymbol{I}$ that is a 10×10 identity matrix.

The layer-wise approach is implemented using interlaminar continuity conditions. These interlaminar continuity conditions are applied to primary variables (u^j, v^j, w^j, ϕ^j and θ^j), transverse shear and transverse normal stresses (σ_{zz}^j, $\sigma_{\alpha z}^j$ and $\sigma_{\beta z}^j$), transverse normal electric displacement ($\mathcal{D}_z^j$) and transverse normal heat flux (q_z^j). Interlaminar continuity conditions allow to link variables between two adjacent j layers. Interlaminar continuity conditions can be written as follows:

$$u_b^j = u_t^{j-1}, \quad v_b^j = v_t^{j-1}, \quad w_b^j = w_t^{j-1}, \quad \phi_b^j = \phi_t^{j-1}, \quad \theta_b^j = \theta_t^{j-1}, \tag{41}$$

$$\sigma_{\alpha z_b}^j = \sigma_{\alpha z_t}^{j-1}, \quad \sigma_{\beta z_b}^j = \sigma_{\beta z_t}^{j-1}, \quad \sigma_{z z_b}^j = \sigma_{z z_t}^{j-1}, \quad \mathcal{D}_{z_b}^j = \mathcal{D}_{z_t}^{j-1}, \quad q_{z_b}^j = q_{z_t}^{j-1}, \tag{42}$$

where a variable at the top (t) of the j-1 layer is equal to the same variable at the bottom (b) of the j layer.

Eqs. (41) and (42) are rewritten in an explicit way by considering Navier harmonic forms (Eqs. (23)–(27)), constitutive Eqs. (1)–(3) and geometrical relations (Eqs. (11)–(12)):

$$\boldsymbol{X}^j(0) = \boldsymbol{T}^{j,j-1} \boldsymbol{X}^{j-1}(h_j), \tag{43}$$

where $\boldsymbol{T}^{j,j-1}$ is the 10×10 *transfer matrix* (from the top of layer $j-1$ to the bottom of layer j) written as:

$$\boldsymbol{T}^{j,j-1} = \begin{bmatrix} 1 & 0 & 0 & 0 & 0 & 0 & 0 & 0 & 0 & 0 \\ 0 & 1 & 0 & 0 & 0 & 0 & 0 & 0 & 0 & 0 \\ 0 & 0 & 1 & 0 & 0 & 0 & 0 & 0 & 0 & 0 \\ 0 & 0 & 0 & 1 & 0 & 0 & 0 & 0 & 0 & 0 \\ 0 & 0 & 0 & 0 & 1 & 0 & 0 & 0 & 0 & 0 \\ T_1 & 0 & T_2 & T_3 & 0 & T_4 & 0 & 0 & 0 & 0 \\ 0 & T_5 & T_6 & T_7 & 0 & 0 & T_8 & 0 & 0 & 0 \\ T_9 & T_{10} & T_{11} & 0 & \tau_1 & 0 & 0 & T_{12} & T_{13} & 0 \\ T_{14} & T_{15} & T_{16} & 0 & \tau_2 & 0 & 0 & T_{17} & T_{18} & 0 \\ 0 & 0 & 0 & 0 & 0 & 0 & 0 & 0 & 0 & \tau_3 \end{bmatrix}^{j,j-1}. \tag{44}$$

The recursive substitution of Eq. (40) into Eq. (43) gives the solution along the $\tilde{z}$ thickness direction for the entire structure. The resulting equation takes the following form:

$$\boldsymbol{X}^M(h_M) = \boldsymbol{A}^{**M} \boldsymbol{T}^{M,M-1} \ldots \boldsymbol{T}^{2,1} \boldsymbol{A}^{**1} \boldsymbol{X}^1(0) = \boldsymbol{H_m} \boldsymbol{X}^1(0). \tag{45}$$

Matrix $\boldsymbol{H_m}$ includes all $\boldsymbol{T}^{j,j-1}$ computed for each interface and $\boldsymbol{A}^{**j}$ matrices computed for each j mathematical layer. Terms in $\boldsymbol{H_m}$

account for geometry dimensions, thickness of each mathematical layer and material layer configuration of the whole structure. The great advantage of this method lies in the constant 10 × 10 dimension of matrix $\boldsymbol{H_m}$ regardless of the N order for the exponential matrix and the total number M of mathematical layers used. This approach enables a very fast computation with modern calculation machines.

Load boundary conditions at the outer surfaces of the structure can be on elastic, thermal and electric fields simultaneously. Four harmonic load combinations can be applied for the present thermal stress analysis. They can be written as follows:

$$\sigma_{zz} = \bar{p}_z, \quad \theta = \bar{\theta}, \quad \phi = \bar{\phi} \text{ for } \tilde{z} = 0, h \,, \tag{46}$$

$$\sigma_{zz} = \bar{p}_z, \quad \theta = \bar{\theta}, \quad \mathcal{D}_z = \bar{\mathcal{D}}_z \text{ for } \tilde{z} = 0, h \,, \tag{47}$$

$$\sigma_{zz} = \bar{p}_z, \quad \bar{q}_z = q_z, \quad \phi = \bar{\phi} \text{ for } \tilde{z} = 0, h \,, \tag{48}$$

$$\sigma_{zz} = \bar{p}_z, \quad \bar{q}_z = q_z, \quad \mathcal{D}_z = \bar{\mathcal{D}}_z \text{ for } \tilde{z} = 0, h \,, \tag{49}$$

where the overbars indicate prescribed values. The explicit form of load boundary conditions in a compact vector and matrix form is:

$$\boldsymbol{B}_b^1 \boldsymbol{X}^1(0) = \boldsymbol{P}_b, \tag{50}$$

$$\boldsymbol{B}_t^M \boldsymbol{X}^M(h_M) = \boldsymbol{P}_t, \tag{51}$$

where $\boldsymbol{B}_b^1$ and $\boldsymbol{B}_t^M$ are the 5 × 10 load boundary condition matrices at the bottom (b) of the first layer (1) and at the top (t) of the last (M) layer; $\boldsymbol{P}_b$ and $\boldsymbol{P}_t$ are the 5 × 1 load vectors at the bottom (b) and at the top (t) of the whole structure.

Considering Eq. (45), it is possible to rewrite Eqs. (50) and (51) as:

$$\begin{bmatrix} \boldsymbol{B}_t^M \boldsymbol{H}_m \\ \boldsymbol{B}_b^1 \end{bmatrix} \boldsymbol{X}_b^1 = \begin{Bmatrix} \boldsymbol{P}_b \\ \boldsymbol{P}_t \end{Bmatrix} \quad \Rightarrow \quad \boldsymbol{E}\boldsymbol{X}^1(0) = \boldsymbol{P}. \tag{52}$$

Matrix $\boldsymbol{E}$ is a 10 × 10 matrix which incorporates all multilayered characteristics. By solving the linear system given in Eq. (52), the 3D solution at the bottom of the structure is obtained. Recursively using Eqs. (40)–(43), the unknown vector along the entire thickness direction $\tilde{z}$ can be evaluated. Once the primary variables are known along the thickness direction $\tilde{z}$, the trends of the secondary variables such as stresses, strains, electric displacement components and heat flux components can be obtained by using Eqs. (1)–(12).

3. Results

This section shows results for the 3D thermal stress analysis of multilayered piezoelectric plates and shells. The results are proposed by using an in-house academic Matlab code (*3DEMS — 3D Exponential Multifield Solutions*) completely developed by the authors. The present 3D analytical model has been named as 3D-u-θ-ϕ. Intuitively, this acronym encloses all the main characteristics of the model: a three-dimensional (3D) thermal stress analysis model where primary variables are displacements (u), over-temperature (θ) and electric potential (ϕ).

This section is divided in two different subsections: in the first one, five validation cases have been considered to evaluate the model and its correctness. In the second subsection, new thermal stress analysis cases are proposed for several multilayered geometries.

3.1. Validation cases

In this subsection, five validation cases for the 3D-u-θ-ϕ model are proposed. Due to a gap in the literature regarding thermal stress analysis for piezoelectric multilayered curved geometries, the thermo-electro-elastic coupling for curved structures has been separately validated considering the thermo-elastic and electro-elastic couplings. For each validation case, a total number of $M = 300$ mathematical layers and $N = 3$ as the order of the exponential matrix have been considered. These two proposed values are derived from an accurate convergence analysis for the static analysis of multilayered structures performed by Brischetto in [46].

The first validation case (VC1) is devoted to a single-layered *Cadmium Selenide* simply-supported plate. The present assessment allows the thermo-electro-elastic coupling validation of the model for a plane structure. Material properties (elastic, electric and thermal ones) of the *Cadmium Selenide* are collected in the first column of Table 1; geometrical properties are explicitly written in the first column of Table 2. Thickness ratios a/h from 2 to 100 are taken into account to validate both thick and thin plate cases. Therefore, both thickness and material layer effects are investigated. The present validation case is divided in two different load boundary conditions: in the first case of Table 3, electric potential at the outer surfaces is imposed in terms of maximum amplitudes $\Phi_t = 10\,\mathrm{V}$ and $\Phi_b = 0\,\mathrm{V}$. In the second one of Table 4, the transverse normal electric displacement at the outer surfaces is imposed in terms of maximum amplitudes $\mathrm{D}_{z_t} = \mathrm{D}_{z_b} = 1\,\mathrm{C/m^2}$. For these two load boundary conditions, no further impositions on elastic and thermal fields are involved. The 3D-u-θ-ϕ model for these two cases is validated considering the 3D analytical thermo-electro-elastic model by Dube et al. [9]. Comparison results of Table 3 are proposed considering the following normalized variables:

$$\bar{u} = \frac{100u}{\frac{a}{h}|d_1|\Phi_t}; \quad \bar{w} = \frac{100w}{|d_1|\Phi_t}; \quad \bar{\sigma}_{\alpha\alpha} = \frac{(\frac{a}{h})^2 h\sigma_{\alpha\alpha}}{E_1|d_1|\Phi_t}; \quad \bar{\sigma}_{\beta\beta} = \frac{h\sigma_{\beta\beta}}{E_1|d_1|\Phi_t}; \quad \bar{\sigma}_{zz} = \frac{(\frac{a}{h})^4 h\sigma_{zz}}{E_1|d_1|\Phi_t};$$
$$\bar{\sigma}_{\alpha z} = \frac{(\frac{a}{h})^3 h\sigma_{\alpha z}}{E_1|d_1|\Phi_t}; \quad \bar{\phi} = \frac{\phi}{\Phi_t}; \quad \bar{D}_z = \frac{hD_z}{d_1^2 E_1 \Phi_t}, \tag{53}$$

where $d_1 = -3.9238 \cdot 10^{-12}\ C/N$ and $E_1 = 42.785 \cdot 10^9$ Pa. Table 3 shows a perfect accordance for each normalized variable proposed. Result accordance is not influenced by the thickness ratio. Table 4 shows a perfect accordance for the second load case too. Normalized variables for these load boundary conditions are the following:

$$\bar{u} = \frac{100|d_1|E_1 u}{\frac{a}{h}h\mathrm{D}_{z_t}}; \quad \bar{w} = \frac{100|d_1|E_1 w}{h\mathrm{D}_{z_t}}; \quad \bar{\sigma}_{\alpha\alpha} = \frac{|d_1|(\frac{a}{h})^2\sigma_{\alpha\alpha}}{\mathrm{D}_{z_t}};$$
$$\bar{\sigma}_{\beta\beta} = \frac{|d_1|\sigma_{\beta\beta}}{\mathrm{D}_{z_t}}; \quad \bar{\sigma}_{zz} = \frac{|d_1|(\frac{a}{h})^4\sigma_{zz}}{\mathrm{D}_{z_t}}; \tag{54}$$
$$\bar{\sigma}_{\alpha z} = \frac{|d_1|(\frac{a}{h})^3\sigma_{\alpha z}}{\mathrm{D}_{z_t}}; \quad \bar{\phi} = \frac{d_1^2 E_1 \phi}{h\mathrm{D}_{z_t}}; \quad \bar{D}_z = \frac{D_z}{\mathrm{D}_{z_t}}.$$

On the basis of the given results, the thermo-electro-elastic coupling is correctly included in the proposed model for both thick and thin plates. Therefore, 3D-u-θ-ϕ model can be considered as validated for plane structures.

The second validation case (VC2) considers the same single-layered simply-supported plate made of *Cadmium Selenide*. Material and geometrical properties are collected in the first column of Table 1 and in the second column of Table 2, respectively. Two different thickness ratios a/h (thick and moderately thick plates) are investigated. This assessment allows the model validation for the thermo-electro-elastic coupling and the material and thickness layer effects in the case of thick plates. For this assessment, the load boundary conditions consider the transverse normal heat flux at the outer surfaces of the plate. Specifically, it has been imposed in terms of maximum amplitudes $Q_{z_t} = 1\,\mathrm{W/m^2}$ and $Q_{z_b} = 0\,\mathrm{W/m^2}$. No loads in terms of pressure and electric potential/electric displacements are applied. In Table 5, the present 3D-u-θ-ϕ model has been compared with the asymptotic results of the 3D sampling surface method by Kulikov [13]. In Table 5, normalized over-temperature, normalized electric potential and normalized in-plane and transverse displacements computed by the 3D-u-θ-ϕ model show a perfect accordance with the reference results in [13]. Normalized terms

Table 1
Elastic, electric and thermal material characteristics used in validation and new benchmark cases.

	Cadmium Selenide	*PZT-5A*	*Aluminum*	*Titanium*	*GR-EP*	*Piezoelectric*
E_1 [GPa]	42.785	61	73	110	172	2
E_2 [GPa]	42.785	61	73	110	6.9	2
E_3 [GPa]	57.707	53.199	73	110	6.9	2
ν_{12} [–]	0.4805	0.35	0.3	0.32	0.25	0.29
ν_{13} [–]	0.2442	0.38	0.3	0.32	0.25	0.29
ν_{23} [–]	0.2442	0.38	0.3	0.32	0.25	0.29
G_{12} [GPa]	14.45	22.593	28.08	41.67	3.4	0.7752
G_{13} [GPa]	13.17	21.1	28.08	41.67	3.4	0.7752
G_{23} [GPa]	13.17	21.1	28.08	41.67	1.4	0.7752
e_{15} [C/m^2]	−0.138	12.322	0	0	0	0
e_{24} [C/m^2]	−0.138	12.322	0	0	0	0
e_{31} [C/m^2]	−0.160	−7.209	0	0	0	0.046
e_{32} [C/m^2]	−0.160	−7.209	0	0	0	0
e_{33} [C/m^2]	0.347	15.118	0	0	0	0
ϵ_1 [nF/m]	0.0825	15.3	0.008854	0.008854	13.060	0.106
ϵ_2 [nF/m]	0.0825	15.3	0.008854	0.008854	13.060	0.106
ϵ_3 [nF/m]	0.0902	15	0.008854	0.008854	13.060	0.106
p [10^{-6} C/m^{2}K]	−2.94	700	0	0	0	N.A.
μ_1 [10^{-6}/K]	1.2566	1.5005	25	8.6	15	120
μ_2 [10^{-6}/K]	1.2566	1.5005	25	8.6	35.3	120
μ_3 [10^{-6}/K]	1.2566	1.9989	25	8.6	35.3	120
k_1 [W/mK]	9	1.8	130	21.9	6	0.19
k_2 [W/mK]	9	1.8	130	21.9	0.56	0.19
k_3 [W/mK]	13.5	1.8	130	21.9	0.56	0.19

N.A: data Not Available.

Table 2
Geometrical data for proposed Validation Cases (VC).

	VC1	VC2	VC3	VC4	VC5
a [m]	1	1	1	$(\pi/3)\cdot R_\alpha$	$(\pi/3)\cdot R_\alpha$
b [m]	1	1	1	1	1
h [m]	Variable	Variable	Variable	Variable	Variable
R_α [m]	∞	∞	∞	10	1
R_β [m]	∞	∞	∞	∞	∞
(m,n)	(1,0)	(1,0)	(1,1)	(1,1)	(1,0)

are here explicitly given:

$$\bar{\theta} = \frac{10hk_0\theta}{a^2 Q_{z_t}};\quad \bar{\phi} = \frac{10^3 k_0 d_0 \phi}{a^2\alpha_0 Q_{z_t}};\quad \bar{u} = \frac{100hk_0 u}{a^3\alpha_0 Q_{z_t}};\quad \bar{w} = \frac{100k_0 w}{a^2\alpha_0 Q_{z_t}}, \tag{55}$$

where $k_0 = 9$ W/mK, $\alpha_0 = 4.396\cdot 10^{-6}$ 1/K and $d_0 = 3.9238\cdot 10^{-12} C/N$. Considering the perfect match with reference results [13], the thermo-electro-elastic coupling, the material and thickness layer effects for thick plates can be considered as validated.

The third validation case (VC3) is about a two-layered *PZT-5A/Cadmium Selenide* (from the bottom to the top) simply-supported square plate. Each material lamina is $0.5h$ where h is the total thickness of the plate. This assessment has been used to validate the model in the case of thermo-electro-elastic coupling in a plane multilayered structure. Material properties for *PZT-5A* and *Cadmium Selenide* can be found in Table 1 (second and first columns). Geometrical plate data are in the third column of Table 2. In the present assessment, load boundary conditions have been imposed in terms of maximum over-temperature amplitudes at the top and bottom plate surfaces. In particular, Θ_t = 1 K and Θ_b = 0 K over-temperature values have been imposed at the external surfaces without any other imposition on electric and elastic fields. Results in Table 6 compare the present 3D-u-θ-ϕ model with the 3D sampling surface method developed by Kulikov [13]. Each normalized variable proposed using the 3D-u-θ-ϕ model is in very good accordance with the reference results by Kulikov [13]. Normalized variables proposed in Table 6 are here shown:

$$\bar{\theta} = \frac{\theta}{\Theta_t};\quad \bar{q}_z = \frac{10aq_z}{\frac{a}{h}k_0\Theta_t};\quad \bar{u} = \frac{10u}{a\alpha_0\Theta_t};\quad \bar{w} = \frac{100w}{\frac{a}{h}a\alpha_0\Theta_t};$$

$$\bar{\sigma}_{\alpha\alpha} = \frac{10\sigma_{\alpha\alpha}}{E_1\alpha_0\Theta_t};\quad \bar{\sigma}_{\alpha\beta} = \frac{10\sigma_{\alpha\beta}}{E_1\alpha_0\Theta_t}; \tag{56}$$

$$\bar{\sigma}_{\alpha z} = \frac{10\frac{a}{h}\sigma_{\alpha z}}{E_1\alpha_0\Theta_t};\quad \bar{\sigma}_{zz} = \frac{10(\frac{a}{h})^2\sigma_{zz}}{E_1\alpha_0\Theta_t}; \tag{57}$$

where $k_0 = 9$ W/mK, $\alpha_0 = 4.396\cdot 10^{-6}$ 1/K and Young Modulus E_1 in Pa is referred to the *Cadmium Selenide*. Results shown in Table 6 allow to attest the validation of the model for the thermo-electro-elastic coupling investigation in the case of multilayered plates.

Validation case number four (VC4) takes into account a two-layered *Aluminum/Titanium* simply-supported cylindrical panel. Each isotropic lamina is $0.5h$ where h is the total thickness of the plate. This assessment is useful to validate the model for the thermo-elastic coupling investigation of curved structures. Material properties for *Aluminum* and *Titanium* have been written in the third and fourth columns of Table 1. Geometrical data for the cylindrical panel are collected in the fourth column of Table 2. Load boundary conditions imposed at the outer surfaces involve the maximum over-temperature amplitudes: Θ_t = 1 K and Θ_b = 0 K without any other imposition on electric and elastic fields. Different thickness ratios in terms of R_α/h are proposed (thick, moderately thick, moderately thin and thin structures). Reference results are the quasi-3D model in [47]. Comparison results proposed in Table 7 show a flawless accordance. For this reason, the thermo-elastic coupling in the proposed model for the case of curved structures can be considered as validated.

In the validation case number five (VC5), a single-layered *Graphite Epoxy Composite (GR-EP)* cylindrical shell with two external *Piezoelectric* patches has been investigated. For this configuration, h_c is the total thickness of the composite lamina (fiber orientation 0°) and $h_p = h_c/100$ is the thickness of each piezoelectric lamina. The total thickness is $h = h_c + 2h_p$. Properties for *GR-EP* and *Piezoelectric* materials are given in the last two columns of Table 1, geometrical data are collected in the last column of Table 2. This assessment has been used to validate the model in the case of electro-elastic coupling in curved structures. The same R_α/h cases investigated in the previous validation example are here proposed. Load boundary conditions imposed at the outer surfaces are in terms of maximum amplitudes for the mechanical transverse normal pressure load: P_{z_t} = 1 Pa and P_{z_b} = 0 Pa without any outer impositions on thermal and electric fields. Reference results come from the 3D model for cylindrical panels developed by Chen et al. [48].

Table 3
VC1. Single-layered *Cadmium Selenide* simply-supported plate in an actuator configuration ($\Phi_t = 10\,\mathrm{V}$, $\Phi_b = 0\,\mathrm{V}$). Thickness coordinate z goes from $-h/2$ to $+h/2$. Tabular results are in terms of the maximum amplitudes at the specific and appropriate points of the $\alpha - \beta$ plane.

a/h		2	4	6	10	20	50	100
$\bar{u}$ $(z=-h/2)$	3D [9]	−4.622	−34.27	−41.19	−44.95	−46.57	−47.04	−47.10
	3D-u-θ-ϕ	−4.622	−34.27	−41.19	−44.95	−46.57	−47.04	−47.10
$\bar{u}$ $(z=+h/2)$	3D [9]	−42.57	−46.26	−46.77	−47.01	−47.09	−47.12	−47.12
	3D-u-θ-ϕ	−42.57	−46.26	−46.77	−47.01	−47.09	−47.12	−47.12
$\bar{w}$ $(z=-h/2)$	3D [9]	234.4	272.5	280.7	285.1	287.0	287.6	287.6
	3D-u-θ-ϕ	234.4	272.5	280.7	285.1	287.0	287.6	287.6
$\bar{w}$ $(z=0)$	3D [9]	168.3	190.7	195.7	198.4	199.6	199.9	200.0
	3D-u-θ-ϕ	168.3	190.7	195.7	198.4	199.6	199.9	200.0
$\bar{w}$ $(z=+h/2)$	3D [9]	62.46	97.36	105.4	109.8	111.6	112.2	112.3
	3D-u-θ-ϕ	62.46	97.36	105.4	109.8	111.6	112.2	112.3
$\bar{\sigma}_{\alpha\alpha}$ $(z=-h/2)$	3D [9]	−4.777	−5.844	−6.079	−6.205	−6.260	−6.275	−6.277
	3D-u-θ-ϕ	−4.778	−5.844	−6.080	−6.205	−6.260	−6.275	−6.277
$\bar{\sigma}_{\alpha\alpha}$ $(z=0)$	3D [9]	2.320	2.903	3.031	3.100	3.129	3.137	3.139
	3D-u-θ-ϕ	2.320	2.903	3.031	3.100	3.129	3.137	3.139
$\bar{\sigma}_{\alpha\alpha}$ $(z=+h/2)$	3D [9]	−5.836	−6.167	−6.229	−6.260	−6.273	−6.277	−6.278
	3D-u-θ-ϕ	−5.836	−6.167	−6.229	−6.263	−6.274	−6.277	−6.278
$\bar{\sigma}_{\beta\beta}$ $(z=-h/2)$	3D [9]	−1.292	−1.092	−1.043	−1.016	−1.004	−1.001	−1.000
	3D-u-θ-ϕ	−1.292	−1.093	−1.043	−1.016	−1.004	−1.001	−1.000
$\bar{\sigma}_{\beta\beta}$ $(z=+h/2)$	3D [9]	−2.362	−1.367	−1.166	−1.060	−1.015	−1.002	−1.001
	3D-u-θ-ϕ	−2.362	−1.367	−1.166	−1.060	−1.015	−1.002	−1.001
$\bar{\sigma}_{zz}$ $(z=0)$	3D [9]	1.498	1.811	1.879	1.915	1.931	1.935	1.936
	3D-u-θ-ϕ	1.498	1.811	1.879	1.915	1.931	1.935	1.936
$\bar{\sigma}_{\alpha z}$ $(z=-h/4)$	3D [9]	1.397	1.719	1.790	1.827	1.844	1.848	1.849
	3D-u-θ-ϕ	1.397	1.719	1.790	1.827	1.844	1.848	1.849
$\bar{\phi}$ $(z=0)$	3D [9]	0.3877	0.4673	0.4850	0.4945	0.4986	0.4998	0.4999
	3D-u-θ-ϕ	0.3877	0.4673	0.4850	0.4945	0.4986	0.4998	0.4999
$\bar{D}_z$ $(z=-h/2)$	3D [9]	−100.2	−129.6	−136.3	−139.9	−141.4	−141.9	−141.9
	3D-u-θ-ϕ	−100.3	−129.6	−136.3	−139.9	−141.4	−141.9	−141.9
$\bar{D}_z$ $(z=+h/2)$	3D [9]	−233.7	−167.2	−153.4	−146.1	−143.0	−142.1	−142.0
	3D-u-θ-ϕ	−233.7	−167.2	−153.4	−146.1	−143.0	−142.1	−142.0

Table 4
VC1. Single-layered *Cadmium Selenide* simply-supported plate in an open circuit configuration ($\mathtt{D}_{z_t} = \mathtt{D}_{z_b} = 1\,\mathrm{C/m^2}$). Thickness coordinate z goes from $-h/2$ to $+h/2$. Tabular results are in terms of the maximum amplitudes at the specific and appropriate points of the $\alpha - \beta$ plane.

a/h		2	4	6	10	20	50	100
$\bar{u}$ $(z=\pm h/2)$	3D [9]	0.1413	0.2713	0.3036	0.3215	0.3293	0.3315	0.3318
	3D-u-θ-ϕ	0.1413	0.2713	0.3036	0.3215	0.3293	0.3315	0.3318
$\bar{w}$ $(z=\pm h/2)$	3D [9]	±0.5148	±0.5899	±0.6051	±0.6131	±0.6165	±0.6175	±0.6176
	3D-u-θ-ϕ	±0.5148	±0.5899	±0.6051	±0.6131	±0.6165	±0.6175	±0.6176
$10^3\bar{\phi}$ $(z=\pm h/2)$	3D [9]	∓2.994	∓3.368	∓3.452	∓3.496	∓3.515	∓3.521	∓3.522
	3D-u-θ-ϕ	∓2.995	∓3.368	∓3.452	∓3.496	∓3.516	∓3.521	∓3.522
$10^3\bar{\sigma}_{\alpha\alpha}$ $(z=\pm h/2)$	3D [9]	31.78	40.46	42.48	43.58	44.06	44.19	44.21
	3D-u-θ-ϕ	31.78	40.46	42.48	43.58	44.06	44.19	44.21
$10^3\bar{\sigma}_{\alpha\alpha}$ $(z=0)$	3D [9]	−13.90	−19.59	−20.92	−21.67	−22.00	−22.09	−22.11
	3D-u-θ-ϕ	−13.90	−19.56	−20.92	−21.67	−22.00	−22.09	−22.11
$10^3\bar{\sigma}_{\beta\beta}$ $(z=\pm h/2)$	3D [9]	10.94	8.285	7.623	7.258	7.098	7.053	7.046
	3D-u-θ-ϕ	10.94	8.285	7.623	7.258	7.098	7.053	7.046

In Table 8, 3D-u-θ-ϕ results are compared with the 3D reference solution [48]. Comparisons made in Table 8 are in good accordance for each proposed normalized variable and for each thickness ratio. Normalization for variables in this assessment are the following:

$$\bar{u} = \frac{100 E_2 u}{h_c (\frac{R_\alpha}{h_c})^4}; \quad \bar{w} = \frac{10 E_2 u}{h_c (\frac{R_\alpha}{h_c})^4}, \tag{58}$$

where E_2 is the Young modulus in Pa for the $GR - EP$ material. On the basis of the results proposed in Table 8, the electro-elastic coupling in the proposed model for curved structures can be considered as validated.

Thanks to the present subsection, the thermo-electro-elastic coupling has been validated in the new proposed model for plane structures. Moreover, the thermo-electro-elastic coupling has also been validated, separately considering thermo-elastic and electro-elastic coupling, in curved structures. Therefore, the thermo-electro-elastic coupling in the proposed new model can be considered as validated for each geometry (both plane and curved ones), thickness value and material lamination. The 3D-u-θ-ϕ model validation has been performed by using $M = 300$ mathematical layers and $N = 3$ order for the exponential matrix. In the next subsection, new cases will be analyzed considering these two values for the 3D-u-θ-ϕ model.

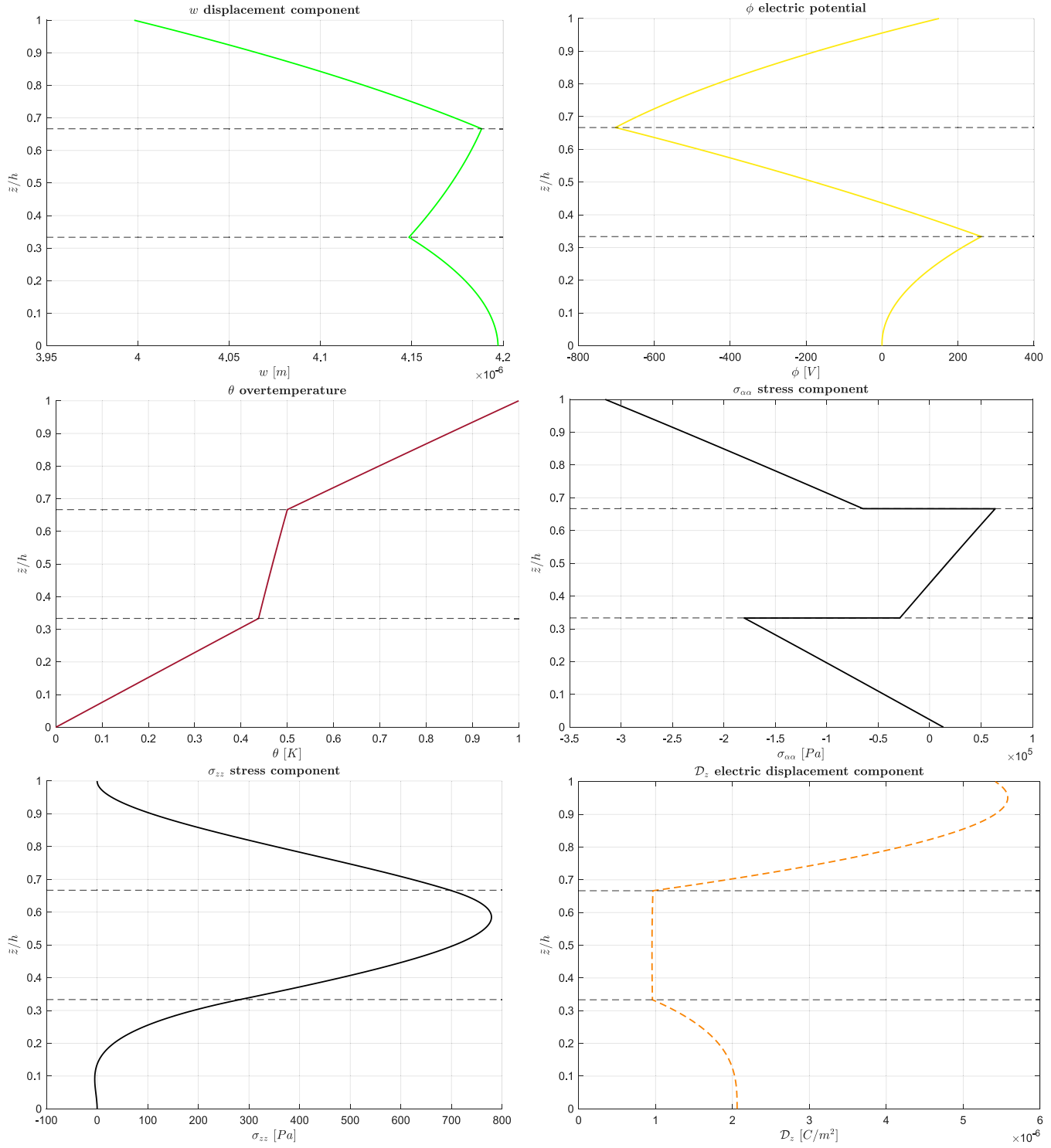

Fig. 2. B1. Graphical trends for the three-layered *PZT-5A/Cadmium Selenide/PZT-5A* simply-supported plate considering Load Boundary conditions LB1 ($\Phi_t = 150\,\mathrm{V}$, $\Phi_b = 0\,\mathrm{V}$ and $\Theta_t = 1\,\mathrm{K}$, $\Theta_b = 0\,\mathrm{K}$). Thickness ratio is $a/h = 10$. Trough-the-thickness variables are in terms of the maximum amplitudes at the specific and appropriate points of the $\alpha - \beta$ plane.

Table 5
VC2. Single-layered *Cadmium Selenide* simply-supported plate with heat flux loads at external surfaces ($Q_{z_t} = 1\,\mathrm{W/m^2}$, $Q_{z_b} = 0\,\mathrm{W/m^2}$). Thickness coordinate z goes from $-h/2$ to $+h/2$. Tabular results are in terms of the maximum amplitudes at the specific and appropriate points of the $\alpha - \beta$ plane.

a/h		2	10
$\bar{\theta}$ $(z = +h/2)$	3D [13]	−1.5160	−1.0353
	3D-u-θ-ϕ	−1.5160	−1.0353
$\bar{\phi}$ $(z = +h/2)$	3D [13]	1.2872	1.3300
	3D-u-θ-ϕ	1.2872	1.3300
$\bar{u}$ $(z = +h/2)$	3D [13]	6.9362	4.7499
	3D-u-θ-ϕ	6.9362	4.7499
$\bar{w}$ $(z = 0)$	3D [13]	−4.0459	−4.8298
	3D-u-θ-ϕ	−4.0459	−4.8298

Table 6
VC3. Two-layered *PZT-5A/Cadmium Selenide* simply-supported plate with over-temperature at external surfaces ($\Theta_t = 1\,\mathrm{K}$, $\Theta_b = 0\,\mathrm{K}$). Thickness coordinate z goes from $-h/2$ to $+h/2$. Tabular results are in terms of the maximum amplitudes at the specific and appropriate points of the $\alpha - \beta$ plane.

a/h		2	10
$\bar{\theta}$ $(z = 0)$	3D [13]	0.60583	0.86748
	3D-u-θ-ϕ	0.60583	0.86748
$\bar{u}$ $(z = +h/2)$	3D [13]	−2.3801	−2.8455
	3D-u-θ-ϕ	−2.3811	−2.8450
$\bar{w}$ $(z = +h/2)$	3D [13]	10.215	6.2730
	3D-u-θ-ϕ	10.243	6.2934
$\bar{\sigma}_{\alpha\alpha}$ $(z = +h/2)$	3D [13]	−4.6432	−1.6989
	3D-u-θ-ϕ	−4.6372	−1.7031
$\bar{\sigma}_{\alpha\beta}$ $(z = +h/2)$	3D [13]	−5.0506	−6.0384
	3D-u-θ-ϕ	−5.0528	−6.0373
$\bar{\sigma}_{\alpha z}$ $(z = 0)$	3D [13]	1.3501	2.7132
	3D-u-θ-ϕ	1.3384	2.6833
$\bar{\sigma}_{zz}$ $(z = 0)$	3D [13]	−1.6477	−6.3876
	3D-u-θ-ϕ	−1.6388	−6.3522
$\bar{q}_z$ $(z = 0)$	3D [13]	−3.3465	−3.5268
	3D-u-θ-ϕ	−3.3465	−3.5268

3.2. New cases

The present subsection focuses on four new cases. Simply-supported multilayered plates, cylinders, cylindrical panels and spherical shells are analyzed. The multilayered configuration is a three-layered configuration *PZT-5A/Cadmium Selenide/PZT-5A* for each analyzed geometry. Elastic, electric and thermal properties for the two materials are collected in Table 1 (first and second columns). Each lamina is $h/3$, considering h as the total thickness of the structure. In each proposed benchmark, two different Load Boundary (LB) conditions are considered in terms of maximum amplitudes:

$$LB1: \ \Theta_t = 1\,\mathrm{K}, \Theta_b = 0\,\mathrm{K}; \ \Phi_t = 150\,\mathrm{V}, \Phi_b = 0\,\mathrm{K}, \tag{59}$$

$$LB2: \ \Theta_t = 1\,\mathrm{K}, \Theta_b = 0\,\mathrm{K}; \ \mathrm{D}_{z_t} = 0.1\,\mathrm{C/m^2}, \mathrm{D}_{z_b} = 0\,\mathrm{C/m^2}. \tag{60}$$

No pressure loads are applied at the outer surfaces. t indicates the top of the geometry ($\tilde{z} = h$), b indicates the bottom of the geometry ($\tilde{z} = 0$). Tabular values and graphical results for both load boundary conditions are obtained by considering $M = 300$ mathematical layers and $N = 3$ order for the exponential matrix (as suggested in the validation cases section).

In the first new case (B1), a multilayered plate structure is proposed. Plate geometrical data are written in the B1 column of Table 9. Thickness ratios from $a/h = 2$ to $a/h = 100$ have been considered. For the LB1 condition, eight different variables (u, w, ϕ, θ, $\sigma_{\alpha\alpha}$, $\sigma_{\beta z}$, σ_{zz}, D_z) are shown in Table 10 at different $\tilde{z}$ locations. For the LB2 condition in Table 11, the following variables are considered at specific thickness coordinate $\tilde{z}$: v, w, ϕ, θ, $\sigma_{\beta\beta}$, $\sigma_{\alpha z}$, σ_{zz}, D_z. For both LB1 and LB2, transverse displacement increases for thin plates while a decreasing trend (from thick to thin structures) for the σ_{zz} stress occurs. For the LB1 configuration, electric potential ϕ increases for thin plates but transverse normal electric displacement D_z decreases. For the LB2 configuration, the opposite trend for these two electric variables occurs. In Fig. 2, graphical trends along the thickness direction for $a/h = 10$ and for w, ϕ, θ, $\sigma_{\alpha\beta}$, σ_{zz} and D_z variables are shown for the LB1 configuration. In Fig. 3, graphical trends for $a/h = 20$ and w, ϕ, θ, $\sigma_{\beta\beta}$, σ_{zz} and D_z are given (LB2 case). The zigzag effect is clearly visible for each variable as the slope changes in correspondence with each physical interface. Physical layer interfaces are highlighted with the dotted horizontal line. In Fig. 2, over-temperature θ and electric potential ϕ have the correct imposed values at the outer surfaces for the LB1 configuration. The same considerations are valid in Fig. 3 for the transverse normal electric displacement D_z and the over-temperature θ. In addition, in both load boundary conditions, the thermo-electro-elastic coupling is clearly visible together with the material and thickness layer effects. Interlaminar continuity conditions are correctly shown as the variables presented in Eqs. (41) and (42) are correctly imposed as continuous along the thickness direction. Variable $\sigma_{\alpha\beta}$ is discontinuous at each physical interface because no interlaminar continuity conditions must be imposed in this case.

The second new case (B2) is devoted to a multilayered cylinder. Geometrical data are collected in Table 9 (second column). Table 12 shows results for several variables considering LB1 conditions and thickness ratios from $R_\alpha/h = 2$ to $R_\alpha/h = 100$. In Table 13, other primary and secondary variables are shown for LB2 conditions considering the same previous thickness ratios. For the LB1 load boundary conditions, u displacement component does not show a monotonous trend for increasing thickness ratios. This peculiarity is due to the curvature effect of the cylinder. Electric variables ϕ and D_z have an opposite trend for higher thickness ratios: ϕ decreases for thinner structures while D_z increases. For the LB2 load boundary conditions, transverse displacement w decreases as the thickness ratio increases. In-plane displacement v and transverse normal stress σ_{zz} do not show a monotonous trend for high R_α/h thickness ratios because of the curvature effects. The two electric variables (ϕ and D_z) have opposite trends for thin cylinders. In Figs. 4 and 5, graphical trends along the thickness direction are shown for LB1 and LB2 conditions, respectively. For the LB1 load boundary conditions, $R_\alpha/h = 4$ has been investigated. For LB2 load boundary conditions, $R_\alpha/h = 10$ is considered. In both cases, the zigzag effect is clearly visible as different slopes occur for different physical layers. For both LB1 and LB2 load boundary conditions, over-temperature θ, electric potential ϕ and transverse normal electric displacement D_z correctly satisfy imposed values at the outer surfaces of the cylinder. Interlaminar continuity conditions are correctly implemented as w, ϕ, θ, σ_{zz} and D_z are continuous along the thickness direction. For each thickness ratio, thermo-electro-elastic coupling, material and thickness layer effects can be clearly seen.

In the third new case (B3), a multilayered cylindrical panel is proposed. Geometrical data can be seen in the third column of Table 9. In Tables 14 and 15, displacements, electric variables and stresses are given at different $\tilde{z}$ locations for six different R_α/h thickness ratios. Both LB1 and LB2 load boundary conditions are investigated. For the LB1 conditions, it can be noted the increasing trend of in-plane displacement, transverse displacement and electric potential and the decreasing trend for electric displacement when thick or thin structures are analyzed. For the LB2 conditions, the same decreasing trend is valid for in-plane and transverse displacements and electric potential; otherwise, the electric displacement increases for thin structures. In Figs. 6 and 7, graphical trends along the thickness direction are shown for LB1 and $R_\alpha/h = 10$ thickness ratio and for LB2 and $R_\alpha/h = 20$ thickness ratio, respectively. All effects discussed in the B2 case are also here valid. The zigzag effect appears as slope changes for each physical layer. Interlaminar continuity conditions are correctly introduced for transverse displacement w, electric potential ϕ, over-temperature θ,

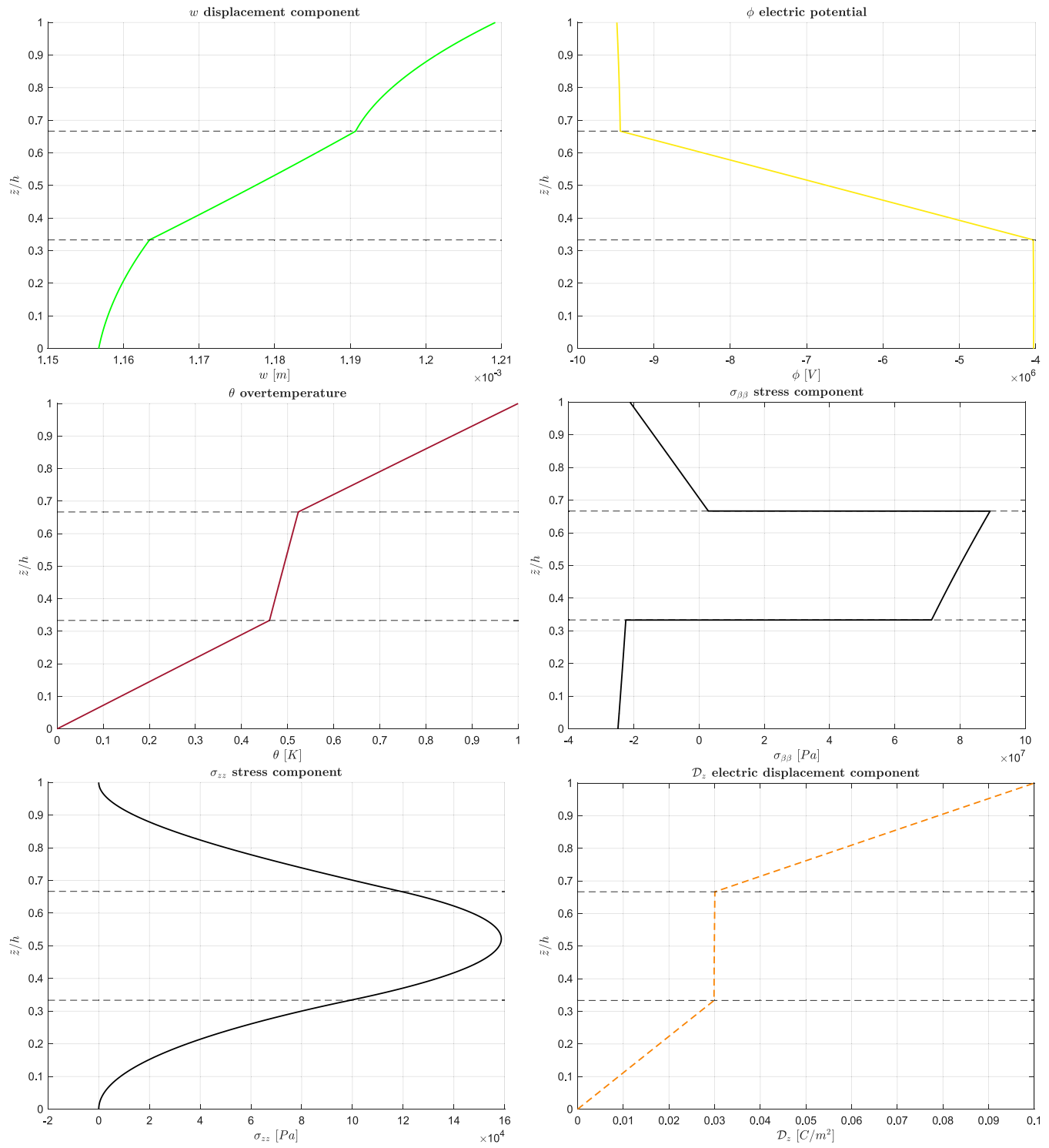

Fig. 3. B1. Graphical trends for the three-layered *PZT-5A/Cadmium Selenide/PZT-5A* simply-supported plate considering Load Boundary conditions LB2 ($\mathtt{D}_{z_t} = 0.1\,\mathrm{C/m^2}$, $\mathtt{D}_{z_t} = 0\,\mathrm{C/m^2}$ and $\Theta_t = 1\,\mathrm{K}$, $\Theta_b = 0\,\mathrm{K}$). Thickness ratio is $a/h = 20$. Trough-the-thickness variables are in terms of the maximum amplitudes at the specific and appropriate points of the $\alpha - \beta$ plane.

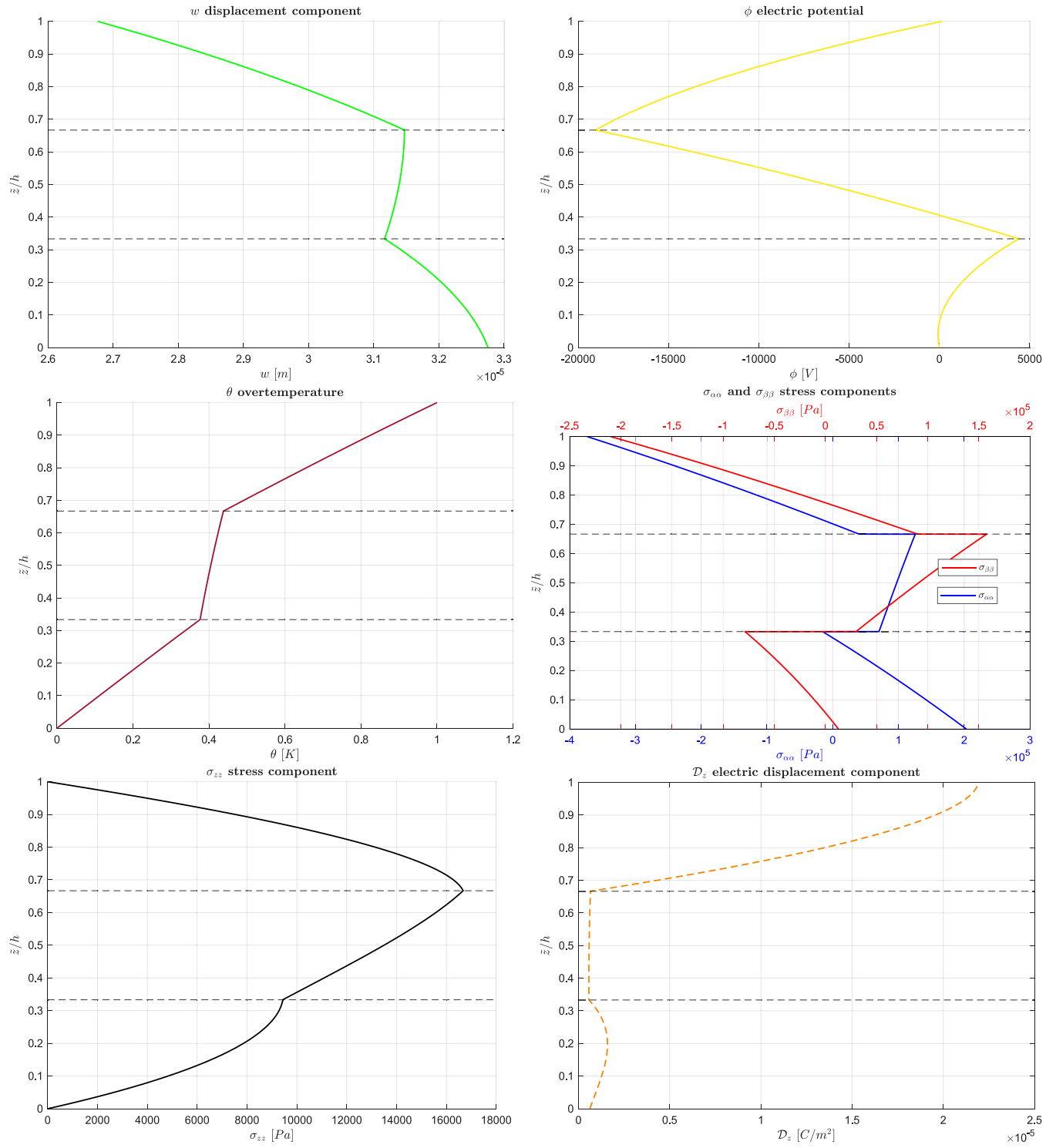

Fig. 4. B2. Graphical trends for the three-layered *PZT-5A/Cadmium Selenide/PZT-5A* simply-supported cylinder considering Load Boundary conditions LB1 ($\Phi_t = 150\,\text{V}$, $\Phi_b = 0\,\text{V}$ and $\Theta_t = 1\,\text{K}$, $\Theta_b = 0\,\text{K}$). Thickness ratio is $R_\alpha/h = 4$. Trough-the-thickness variables are in terms of the maximum amplitudes at the specific and appropriate points of the $\alpha - \beta$ plane.

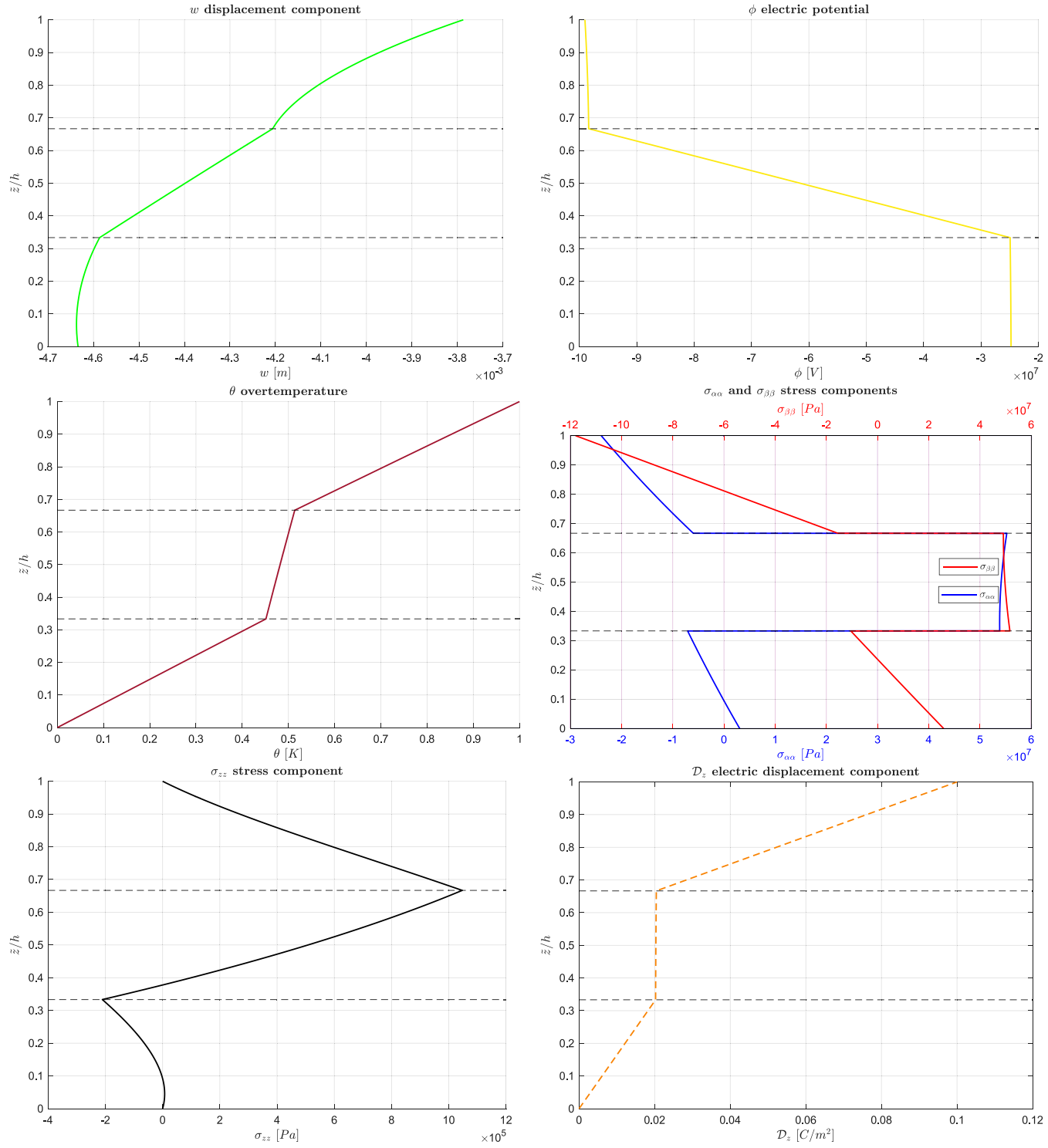

Fig. 5. B2. Graphical trends for the three-layered *PZT-5A/Cadmium Selenide/PZT-5A* simply-supported cylinder considering Load Boundary conditions LB2 ($\mathtt{D}_{z_t} = 0.1\,\mathrm{C/m^2}$, $\mathtt{D}_{z_b} = 0\,\mathrm{C/m^2}$ and $\Theta_t = 1\,\mathrm{K}$, $\Theta_b = 0\,\mathrm{K}$). Thickness ratio is $R_\alpha/h = 10$. Trough-the-thickness variables are in terms of the maximum amplitudes at the specific and appropriate points of the $\alpha - \beta$ plane.

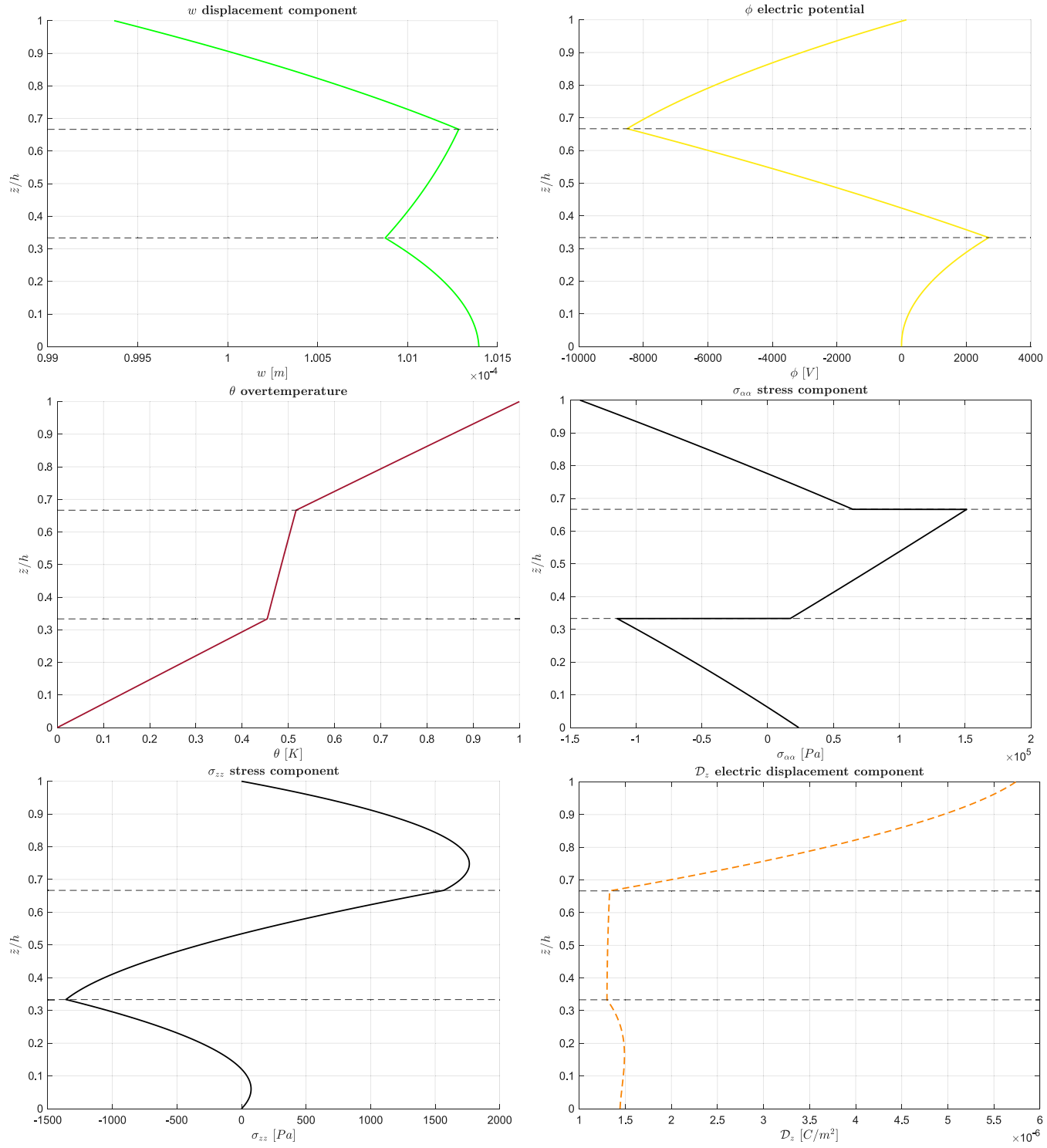

Fig. 6. B3. Graphical trends for the three-layered *PZT-5A/Cadmium Selenide/PZT-5A* simply-supported cylindrical panel considering Load Boundary conditions LB1 ($\Phi_t = 150\,\text{V}$, $\Phi_b = 0\,\text{V}$ and $\Theta_t = 1\,\text{K}$, $\Theta_b = 0\,\text{K}$). Thickness ratio is $R_\alpha/h = 10$. Trough-the-thickness variables are in terms of the maximum amplitudes at the specific and appropriate points of the $\alpha - \beta$ plane.

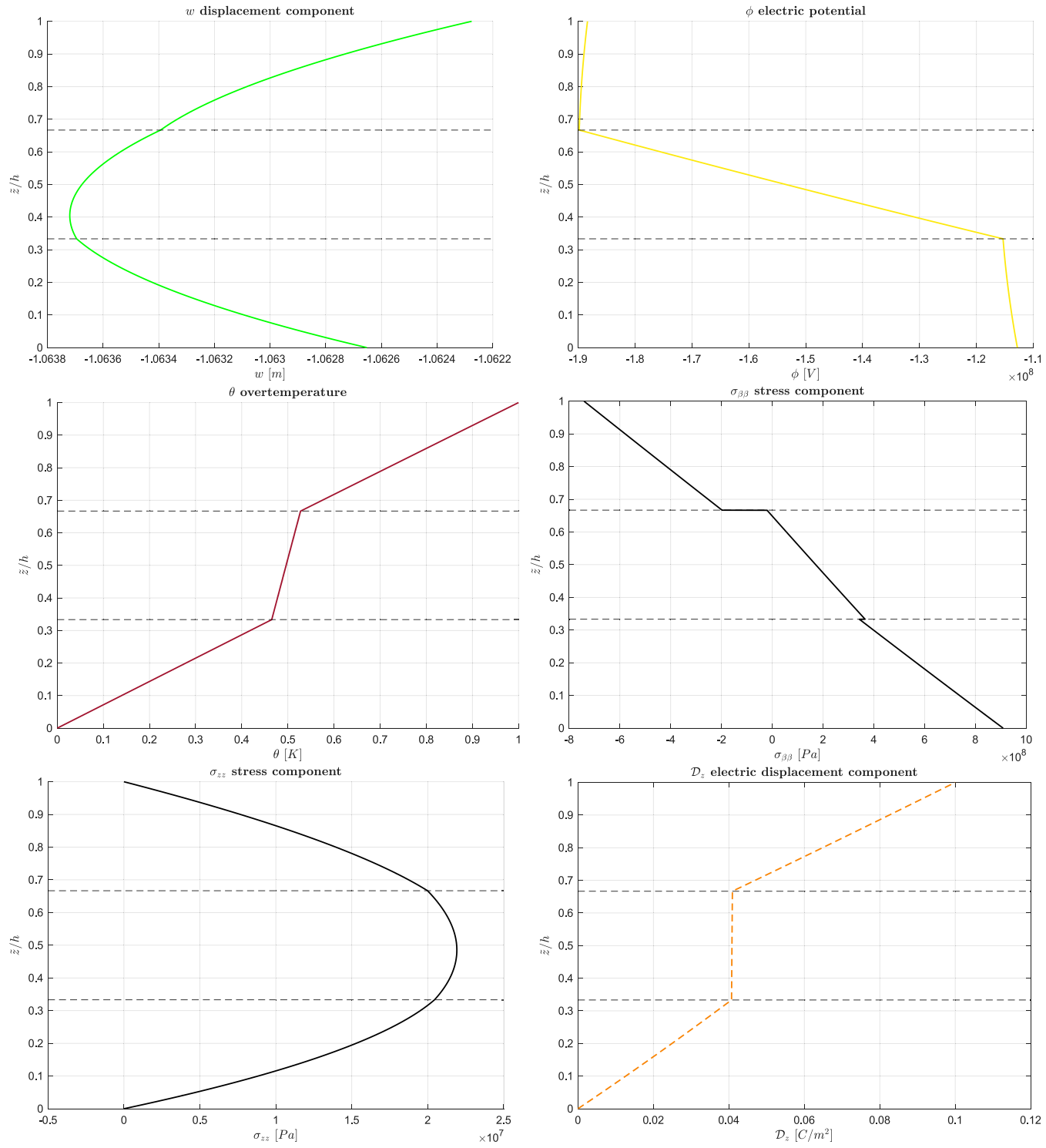

Fig. 7. B3. Graphical trends for the three-layered *PZT-5A/Cadmium Selenide/PZT-5A* simply-supported cylindrical panel considering Load Boundary conditions LB2 ($\mathtt{D}_{z_t} = 0.1\,\mathrm{C/m^2}$, $\mathtt{D}_{z_b} = 0\,\mathrm{C/m^2}$ and $\Theta_t = 1\,\mathrm{K}$, $\Theta_b = 0\,\mathrm{K}$). Thickness ratio is $R_a/h = 20$. Trough-the-thickness variables are in terms of the maximum amplitudes at the specific and appropriate points of the $\alpha - \beta$ plane.

Table 7
VC4. Two-layered *Aluminum/Titanium* simply-supported cylindrical shell with over-temperature at external surfaces ($\Theta_t = +1\,\mathrm{K}$ and $\Theta_b = 0\,\mathrm{K}$). Thickness coordinate z goes from $-h/2$ to $+h/2$. Tabular results are in terms of the maximum amplitudes at the specific and appropriate points of the $\alpha - \beta$ plane.

R_α/h		5	10	50	100	1000
$w[10^{-3}m]$ $(z=0)$	Quasi-3D [47]	0.0002	0.0010	0.0060	0.0129	0.0424
	3D-u-θ-ϕ	0.0002	0.0010	0.0060	0.0129	0.0424
$u[10^{-4}m]$ $(z=+h/2)$	Quasi-3D [47]	−0.0031	−0.0031	−0.0027	−0.0023	0.0009
	3D-u-θ-ϕ	−0.0031	−0.0031	−0.0027	−0.0023	0.0009

Table 8
VC5. Single-layered *composite GR-EP* simply-supported cylindrical shell with two external *Piezoelectric* patches in sensor configuration ($P_{z_t} = 1\,\mathrm{Pa}$, $P_{z_b} = 0\,\mathrm{Pa}$). Thickness coordinate z goes from $-h/2$ to $+h/2$. Tabular results are in terms of the maximum amplitudes at the specific and appropriate points of the $\alpha - \beta$ plane.

R_α/h		2	4	10	50	100
$\bar{u}$ $(z=+h/2)$	3D [48]	3.380	1.030	0.374	0.251	0.247
	3D-u-θ-ϕ	3.495	1.062	0.384	0.257	0.252
$\bar{w}$ $(z=+h/2)$	3D [48]	0.981	0.306	0.112	0.0754	0.0740
	3D-u-θ-ϕ	1.015	0.316	0.115	0.0772	0.0757

Table 9
Geometrical data for new proposed Benchmarks (B).

	B1	B2	B3	B4
a [m]	1	$2\pi R_\alpha$	$(\pi/3)\cdot R_\alpha$	$(\pi/3)\cdot R_\alpha$
b [m]	1	10	1	$(\pi/3)\cdot R_\beta$
h [m]	Variable	Variable	Variable	Variable
R_α [m]	∞	10	10	10
R_β [m]	∞	∞	∞	10
(m,n)	(1,1)	(2,1)	(1,0)	(1,1)

transverse normal stress σ_{zz}, transverse normal electric displacement D_z: they are continuous along the thickness direction. Load boundary conditions LB1 and LB2 have always been correctly imposed at the outer surfaces. Thermo-electro-elastic coupling, material and thickness layer effects are also clearly shown in graphical trends for these new cases.

In the last benchmark (B4), a multilayered spherical shell is analyzed. Geometrical data are collected in Table 9 (last column). Tables 16 and 17 show primary and secondary variables at different thickness locations in the case of several R_α/h thickness ratios. Table 16 is for the LB1 configuration at fixed $\tilde{z}$ values. Table 17 investigates variables at fixed $\tilde{z}$ values for the LB2 configuration. For the LB1 conditions, the curvature effect is visible in the transverse normal displacement w trend for increasing R_α/h values: a non-monotonous trend is clearly shown. Electric variables have an opposite trend for higher thickness ratios: ϕ increases and D_z decreases for thin structures. As concerns trends for the LB2 conditions, v, w and ϕ primary variables decrease for higher thickness ratios. On the contrary, D_z electric displacement increases for higher R_α/h values. In Fig. 8, graphical trends along the thickness direction (considering the LB1 load boundary conditions) are shown for a thick spherical shell ($R_\alpha/h = 4$). In Fig. 8, the thickness layer effect is clear because of the high thickness ratio R_α/h proposed. In Fig. 9, the same variables are proposed for the LB2 load boundary configuration for a moderately thin spherical shell ($R_\alpha/h = 50$). In both figures, all involved effects can be noted. Thermo-electro-elastic coupling is correctly shown for both load boundary configurations. Variables θ, ϕ and D_z perfectly satisfy the imposed values at the outer surfaces for both load boundary conditions. Change in slope and interlaminar continuity are correctly captured at each physical interface for both cases.

The four proposed benchmarks, as shown through the graphical results, illustrate the influence of thermo-electro-elastic coupling on the structural behavior of plates and shells. The elastic and static response of a structure depends not only on mechanical loads but also on applied temperature and electric potential profiles, which induce additional strains and stresses beyond the classical elastic ones. Notably, this behavior differs between plates and shells, as the presence of curvature in shells introduces further couplings between in-plane and out-of-plane components of the elastic, thermal, and electrical variables. These multi-field coupling effects are already evident at the level of the governing and constitutive equations, highlighting the interactions among the different physical fields. At the same time, curvature effects manifest in the geometric equations, adding further coupling terms absent in flat geometries, thereby emphasizing the distinct structural response of shells compared to plates.

4. Conclusions

The present paper investigates the 3D thermal stress analysis of simply-supported multilayered piezoelectric curved structures. In the present 3D thermal stress analysis, the three 3D equilibrium equations, the 3D divergence equation for the electric displacement and the 3D Fourier heat conduction equation for spherical shells are solved using the orthogonal mixed curvilinear reference system. The methodology involves the Navier harmonic forms in the in-plane directions for displacements, electric potential and over-temperature, and the exponential matrix method in the thickness direction. This model correctly implements the layer-wise approach thanks to the introduction of the interlaminar continuity conditions. Several loading boundary conditions have been investigated considering coupled or partially coupled thermal, electric and elastic fields.

The main innovation includes the use of a general methodology to perform the 3D thermal stress analysis for different multilayered piezoelectric structures (cylinders, cylindrical panels, spherical shells and plates) with a unique set of 3D equations coupling elastic, electric and thermal fields. The present model shows accurate 3D trends along the thickness direction for all elastic, electric and thermal variables.

In the results section, the preliminary validation confirms the correctness of the present 3D model. Numerical comparisons with other 3D thermo-electro-elastic models have been performed in terms of displacements, stresses, electric potential, electric displacement and over-temperature. All the involved effects, such as the zigzag effect, thermo-electro-elastic coupling, material layer effect, thickness layer effect, and curvature effect, are correctly evaluated for all cases. These effects are accurately described in 3D form.

New cases have been investigated involving plate and shell geometries for two different loading boundary conditions and various thickness ratios. The new cases here proposed are useful for those scientists involved in the study and numerical evaluation of the behavior of intelligent structures for aerospace purposes or for those researchers involved in the development of analytical and numerical models of multilayered smart structures.

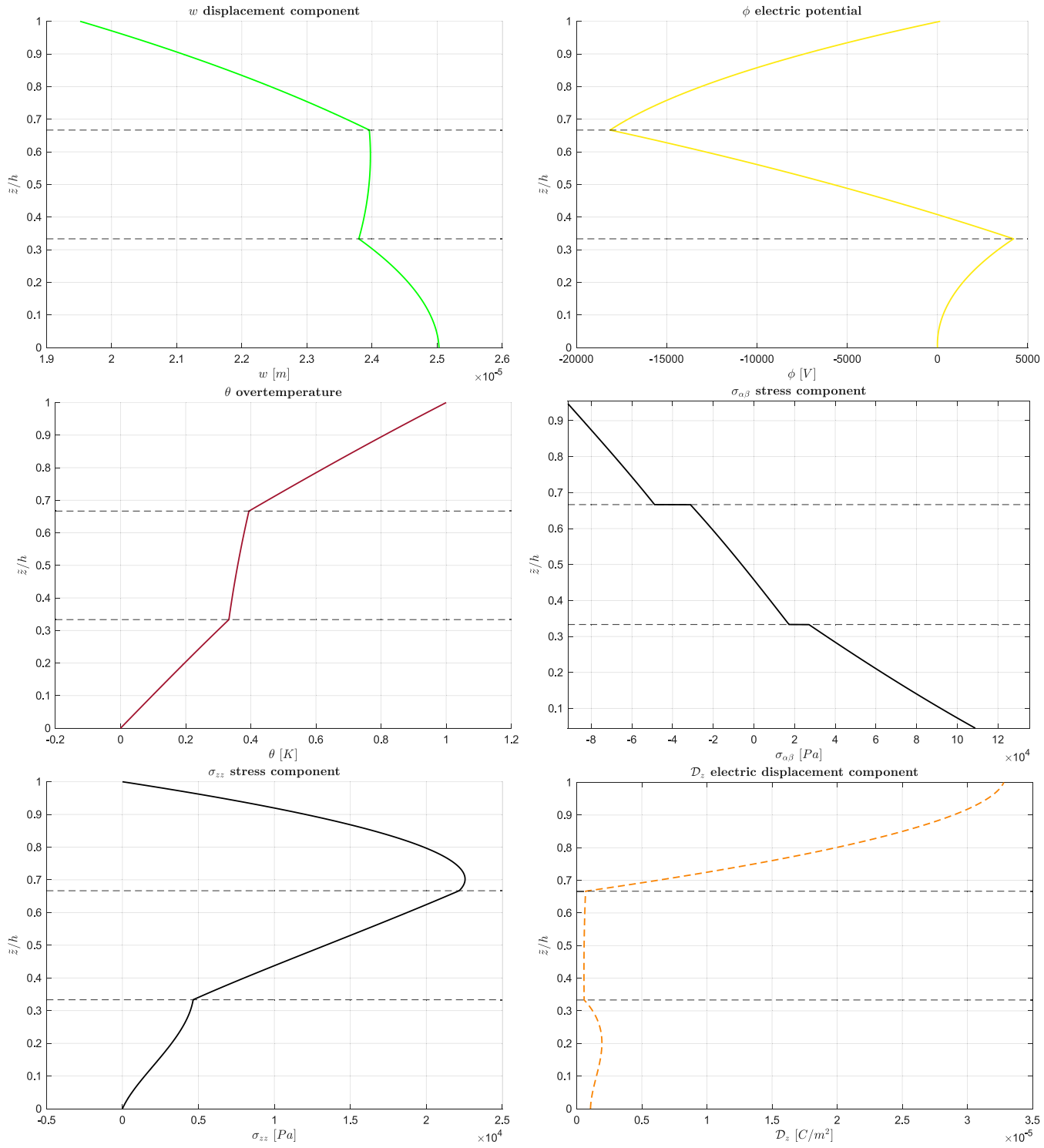

Fig. 8. B4. Graphical trends for the three-layered *PZT-5A/Cadmium Selenide/PZT-5A* simply-supported spherical shell considering Load Boundary conditions LB1 ($\Phi_t = 150\,\text{V}$, $\Phi_b = 0\,\text{V}$ and $\Theta_t = 1\,\text{K}$, $\Theta_b = 0\,\text{K}$). Thickness ratio is $R_\alpha/h = 4$. Trough-the-thickness variables are in terms of the maximum amplitudes at the specific and appropriate points of the $\alpha - \beta$ plane.

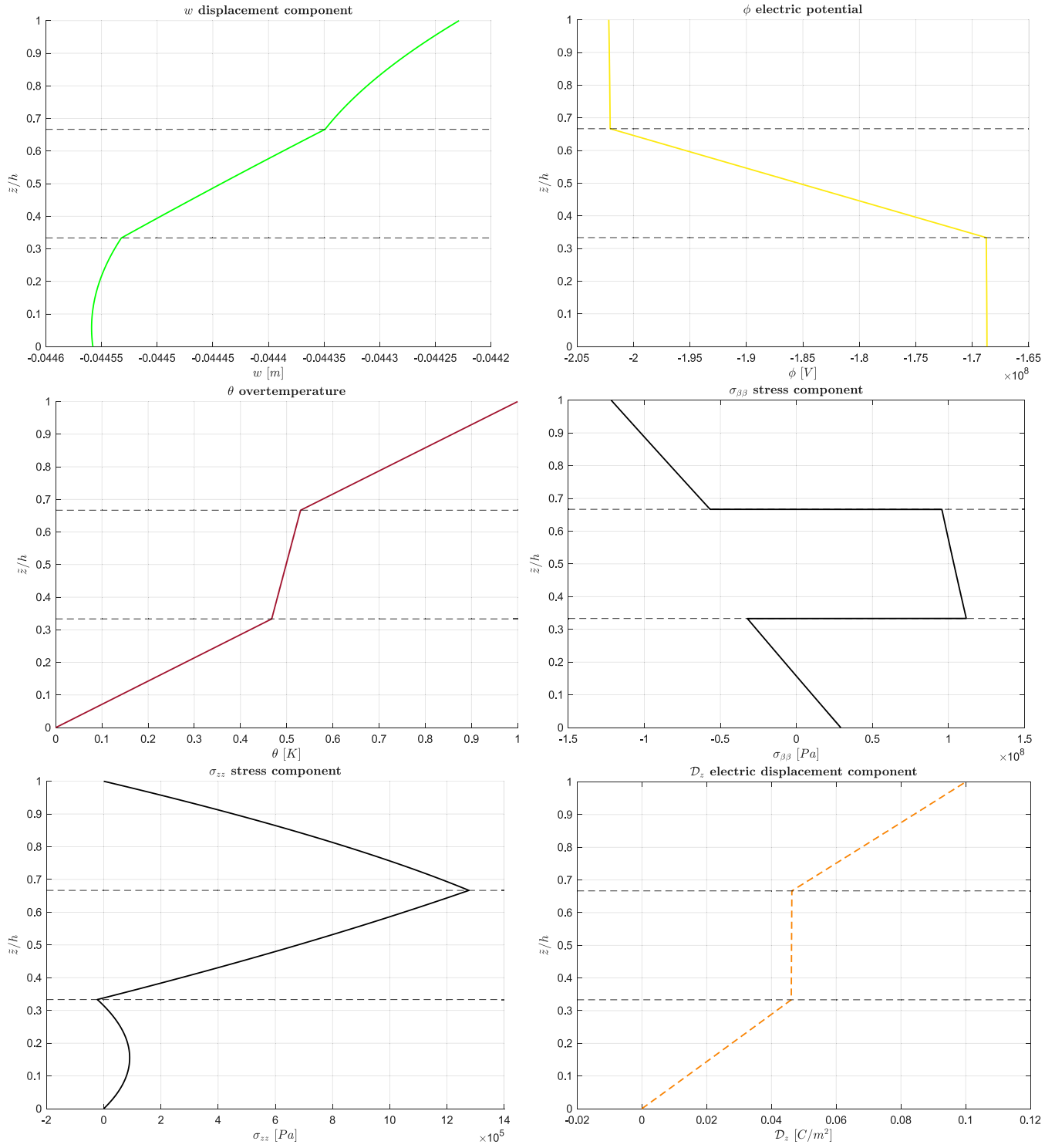

Fig. 9. B4. Graphical trends for the three-layered *PZT-5A/Cadmium Selenide/PZT-5A* simply-supported spherical shell considering Load Boundary conditions LB2 ($\mathtt{D}_{z_t} = 0.1\,\mathrm{C/m^2}$, $\mathtt{D}_{z_b} = 0\,\mathrm{C/m^2}$ and $\Theta_t = 1\,\mathrm{K}$, $\Theta_b = 0\,\mathrm{K}$). Thickness ratio is $R_\alpha/h = 50$. Trough-the-thickness variables are in terms of the maximum amplitudes at the specific and appropriate points of the $\alpha - \beta$ plane.

Table 10
B1. Three-layered *PZT-5A/Cadmium Selenide/PZT-5A* simply-supported plate considering Load Boundary conditions LB1 ($\Phi_t = 150\,\mathrm{V}$, $\Phi_b = 0\,\mathrm{V}$ and $\Theta_t = 1\,\mathrm{K}$, $\Theta_b = 0\,\mathrm{K}$). Thickness coordinate $\bar{z}$ goes from 0 to h. Tabular results are in terms of the maximum amplitudes at the specific and appropriate points of the $\alpha - \beta$ plane.

a/h	2	4	10	20	50	100
			$u\,[10^{-6}\,\mathrm{m}]$ $(\bar{z}/h = 1.00)$			
	−0.8395	−1.1395	−1.3173	−1.3504	−1.3635	−1.3722
			$w\,[10^{-6}\,\mathrm{m}]$ $(\bar{z}/h = 1.00)$			
	0.5535	1.4005	3.9981	8.1766	20.583	41.214
			$\phi\,[\mathrm{V}]$ $(\bar{z}/h = 0.50)$			
	−877.20	−517.09	−178.40	−52.815	23.786	49.394
			$\theta\,[\mathrm{K}]$ $(\bar{z}/h = 0.50)$			
	0.1743	0.3488	0.4682	0.4917	0.4987	0.4997
			$\sigma_{\alpha\alpha}\,[10^{4}\,\mathrm{Pa}]$ $(\bar{z}/h = 0.00)$			
	−8.7313	−3.0918	1.3376	2.2309	2.5521	2.7005
			$\sigma_{\beta z}\,[10^{3}\,\mathrm{Pa}]$ $(\bar{z}/h = 0.50)$			
	13.335	6.5325	2.5561	1.2743	0.5096	0.2549
			$\sigma_{zz}\,[\mathrm{Pa}]$ $(\bar{z}/h = 0.50)$			
	31 585	6168.5	706.88	160.99	24.238	5.6698
			$\mathcal{D}_z\,[10^{-6}\,\mathrm{C/m^2}]$ $(\bar{z}/h = 1.00)$			
	103.73	32.688	5.4185	1.1689	−0.8243	−2.8715

Table 11
B1. Three-layered *PZT-5A/Cadmium Selenide/PZT-5A* simply-supported plate considering Load Boundary conditions LB2 ($\mathrm{D}_{z_t} = 0.1\,\mathrm{C/m^2}$, $\mathrm{D}_{z_t} = 0\,\mathrm{C/m^2}$ and $\Theta_t = 1\,\mathrm{K}$, $\Theta_b = 0\,\mathrm{K}$). Thickness coordinate $\bar{z}$ goes from 0 to h. Tabular results are in terms of the maximum amplitudes at the specific and appropriate points of the $\alpha - \beta$ plane.

a/h	2	4	10	20	50	100
			$v\,[10^{-4}\,\mathrm{m}]$ $(\bar{z}/h = 1.00)$			
	2.4936	2.6654	2.7768	2.8813	2.9740	2.9953
			$w\,[10^{-4}\,\mathrm{m}]$ $(\bar{z}/h = 1.00)$			
	2.4558	3.0589	6.3118	12.092	29.584	58.913
			$\phi\,[10^{5}\,\mathrm{V}]$ $(\bar{z}/h = 0.00)$			
	0.0494	−0.6125	−9.0105	−40.270	−152.22	−328.35
			$\theta\,[\mathrm{K}]$ $(\bar{z}/h = 0.50)$			
	0.1743	0.3488	0.4682	0.4917	0.4987	0.4997
			$\sigma_{\beta\beta}\,[10^{7}\,\mathrm{Pa}]$ $(\bar{z}/h = 0.00)$			
	−1.4556	−1.7844	−2.1021	−2.4891	−2.8424	−2.9242
			$\sigma_{\alpha z}\,[10^{5}\,\mathrm{Pa}]$ $(\bar{z}/h = 0.50)$			
	18.083	11.192	4.7686	2.4062	0.9650	0.4827
			$\sigma_{zz}\,[10^{5}\,\mathrm{Pa}]$ $(\bar{z}/h = 0.50)$			
	45.859	16.088	4.1380	1.5788	0.3329	0.0879
			$\mathcal{D}_z\,[10^{-2}\,\mathrm{C/m^2}]$ $(\bar{z}/h = 0.50)$			
	0.0655	0.2716	1.3534	2.9939	4.5165	4.8697

Table 12
B2. Three-layered *PZT-5A/Cadmium Selenide/PZT-5A* simply-supported cylinder considering Load Boundary conditions LB1 ($\Phi_t = 150\,\mathrm{V}$, $\Phi_b = 0\,\mathrm{V}$ and $\Theta_t = 1\,\mathrm{K}$, $\Theta_b = 0\,\mathrm{K}$). Thickness coordinate $\bar{z}$ goes from 0 to h. Tabular results are in terms of the maximum amplitudes at the specific and appropriate points of the $\alpha - \beta$ plane.

R_α/h	2	4	10	20	50	100
			$u\,[10^{-6}\,\mathrm{m}]$ $(\bar{z}/h = 1.00)$			
	−1.9908	−0.2516	2.4653	3.1175	3.1989	3.1638
			$w\,[10^{-5}\,\mathrm{m}]$ $(\bar{z}/h = 1.00)$			
	1.3962	2.6761	3.6829	3.6923	3.5325	3.4535
			$\phi\,[10^{3}\,\mathrm{V}]$ $(\bar{z}/h = 0.50)$			
	−10.599	−6.2697	−3.0831	−1.6677	−0.6598	−0.2980
			$\theta\,[\mathrm{K}]$ $(\bar{z}/h = 0.50)$			
	0.2523	0.4046	0.4820	0.4954	0.4993	0.4998
			$\sigma_{\alpha\alpha}\,[10^{5}\,\mathrm{Pa}]$ $(\bar{z}/h = 0.00)$			
	0.8528	2.0326	3.2991	3.6465	3.7469	3.7577
			$\sigma_{\alpha\beta}\,[10^{3}\,\mathrm{Pa}]$ $(\bar{z}/h = 0.50)$			
	−1.3148	1.4070	6.0812	4.6765	2.2678	1.2004
			$\sigma_{zz}\,[10^{3}\,\mathrm{Pa}]$ $(\bar{z}/h = 0.50)$			
	34.763	13.495	6.1016	3.3944	1.4407	0.7327
			$\mathcal{D}_z\,[10^{-6}\,\mathrm{C/m^2}]$ $(\bar{z}/h = 1.00)$			
	70.539	21.920	4.3361	1.5590	0.6174	0.2739

Table 13
B2. Three-layered *PZT-5A/Cadmium Selenide/PZT-5A* simply-supported cylinder considering Load Boundary conditions LB2 ($\mathtt{D}_{z_t} = 0.1\,\mathrm{C/m^2}$, $\mathtt{D}_{z_b} = 0\,\mathrm{C/m^2}$ and $\Theta_t = 1\,\mathrm{K}$, $\Theta_b = 0\,\mathrm{K}$). Thickness coordinate $\tilde{z}$ goes from 0 to h. Tabular results are in terms of the maximum amplitudes at the specific and appropriate points of the $\alpha - \beta$ plane.

R_α/h	2	4	10	20	50	100
			$v\,[10^{-4}\,\mathrm{m}]$ $(\tilde{z}/h = 0.00)$			
	3.0746	−2.5725	−11.740	−12.128	−3.1629	11.507
			$w\,[10^{-3}\,\mathrm{m}]$ $(\tilde{z}/h = 0.00)$			
	0.7940	0.1198	−4.6339	−10.377	−19.312	−30.935
			$\phi\,[10^{7}\,\mathrm{V}]$ $(\tilde{z}/h = 0.00)$			
	−0.0197	−0.2323	−2.4779	−8.9661	−28.933	−60.358
			$\theta\,[\mathrm{K}]$ $(\tilde{z}/h = 0.50)$			
	0.2523	0.4046	0.4820	0.4954	0.4993	0.4998
			$\sigma_{\beta\beta}\,[10^{7}\,\mathrm{Pa}]$ $(\tilde{z}/h = 1.00)$			
	−5.6048	−8.0984	−11.799	−13.583	−15.380	−18.059
			$\sigma_{\alpha z}\,[10^{6}\,\mathrm{Pa}]$ $(\tilde{z}/h = 0.50)$			
	−2.3825	−3.3851	−2.5817	−1.2839	−0.3693	−0.1460
			$\sigma_{zz}\,[10^{5}\,\mathrm{Pa}]$ $(\tilde{z}/h = 0.50)$			
	17.011	8.5979	5.0811	2.5148	0.7896	0.3369
			$\mathcal{D}_z\,[10^{-2}\,\mathrm{C/m^2}]$ $(\tilde{z}/h = 0.50)$			
	0.1223	0.4846	2.0327	3.6686	4.7292	4.9311

Table 14
B3. Three-layered *PZT-5A/Cadmium Selenide/PZT-5A* simply-supported cylindrical panel considering Load Boundary conditions LB1 ($\Phi_t = 150\,\mathrm{V}$, $\Phi_b = 0\,\mathrm{V}$ and $\Theta_t = 1\,\mathrm{K}$, $\Theta_b = 0\,\mathrm{K}$). Thickness coordinate $\tilde{z}$ goes from 0 to h. Tabular results are in terms of the maximum amplitudes at the specific and appropriate points of the $\alpha - \beta$ plane.

R_α/h	2	4	10	20	50	100
			$u\,[10^{-5}\,\mathrm{m}]$ $(\tilde{z}/h = 1.00)$			
	−1.9107	−1.4747	0.4756	3.7901	13.717	30.408
			$w\,[10^{-5}\,\mathrm{m}]$ $(\tilde{z}/h = 1.00)$			
	1.5482	3.8212	9.9370	19.857	49.607	99.688
			$\phi\,[10^{3}\,\mathrm{V}]$ $(\tilde{z}/h = 0.50)$			
	−10.982	−6.0232	−2.4740	−1.2136	−0.4425	−0.1833
			$\theta\,[\mathrm{K}]$ $(\tilde{z}/h = 0.50)$			
	0.2793	0.4191	0.4851	0.4962	0.4994	0.4998
			$\sigma_{\alpha\alpha}\,[10^{4}\,\mathrm{Pa}]$ $(\tilde{z}/h = 0.00)$			
	−14.265	−3.3336	2.3573	3.6107	4.0682	4.0173
			$\sigma_{\alpha z}\,[10^{3}\,\mathrm{Pa}]$ $(\tilde{z}/h = 0.50)$			
	3.8771	3.4157	1.5456	0.7993	0.3414	0.1878
			$\sigma_{zz}\,[10^{2}\,\mathrm{Pa}]$ $(\tilde{z}/h = 0.50)$			
	112.78	7.7065	−3.2337	−2.2470	−1.0731	−0.6088
			$\mathcal{D}_z\,[10^{-6}\,\mathrm{C/m^2}]$ $(\tilde{z}/h = 1.00)$			
	53.224	20.193	5.7369	2.8464	1.6400	1.1867

Table 15
B3. Three-layered *PZT-5A/Cadmium Selenide/PZT-5A* simply-supported cylindrical panel considering Load Boundary conditions LB2 ($\mathtt{D}_{z_t} = 0.1\,\mathrm{C/m^2}$, $\mathtt{D}_{z_b} = 0\,\mathrm{C/m^2}$ and $\Theta_t = 1\,\mathrm{K}$, $\Theta_b = 0\,\mathrm{K}$). Thickness coordinate $\tilde{z}$ goes from 0 to h. Tabular results are in terms of the maximum amplitudes at the specific and appropriate points of the $\alpha - \beta$ plane.

R_α/h	2	4	10	20	50	100
			$u\,[\mathrm{m}]$ $(\tilde{z}/h = 1.00)$			
	0.0069	0.0064	−0.0177	−0.2811	−5.2928	−44.300
			$w\,[\mathrm{m}]$ $(\tilde{z}/h = 1.00)$			
	0.0030	−0.0001	−0.1120	−1.0623	−17.241	−138.38
			$\phi\,[10^{7}\,\mathrm{V}]$ $(\tilde{z}/h = 0.00)$			
	−0.0328	−0.3265	−3.2827	−11.282	−35.332	−73.392
			$\theta\,[\mathrm{K}]$ $(\tilde{z}/h = 0.50)$			
	0.2793	0.4191	0.4851	0.4962	0.4994	0.4998
			$\sigma_{\beta\beta}\,[10^{8}\,\mathrm{Pa}]$ $(\tilde{z}/h = 0.00)$			
	−0.0563	0.2106	2.1700	9.0941	55.765	219.66
			$\sigma_{\alpha z}\,[10^{7}\,\mathrm{Pa}]$ $(\tilde{z}/h = 0.50)$			
	−0.6633	−1.3698	−3.4033	−6.7555	−16.850	−33.688
			$\sigma_{zz}\,[10^{6}\,\mathrm{Pa}]$ $(\tilde{z}/h = 0.50)$			
	1.7286	2.6337	9.9030	21.906	56.053	112.27
			$\mathcal{D}_z\,[10^{-3}\,\mathrm{C/m^2}]$ $(\tilde{z}/h = 0.50)$			
	1.9687	6.6135	24.230	40.825	52.501	58.494

Table 16
B4. Three-layered *PZT-5A/Cadmium Selenide/PZT-5A* simply-supported spherical shell considering Load Boundary conditions LB1 ($\Phi_t = 150\,\mathrm{V}$, $\Phi_b = 0\,\mathrm{V}$ and $\Theta_t = 1\,\mathrm{K}$, $\Theta_b = 0\,\mathrm{K}$). Thickness coordinate $\tilde{z}$ goes from 0 to h. Tabular results are in terms of the maximum amplitudes at the specific and appropriate points of the $\alpha - \beta$ plane.

R_α/h	2	4	10	20	50	100
			$u\,[10^{-6}\,\mathrm{m}]$ $(\tilde{z}/h = 1.00)$			
	−8.7232	−8.2835	−3.9500	−1.4773	−0.3652	−0.1370
			$w\,[10^{-5}\,\mathrm{m}]$ $(\tilde{z}/h = 1.00)$			
	0.8981	1.9517	3.2558	3.4347	3.2795	3.1784
			$\phi\,[10^{3}\,\mathrm{V}]$ $(\tilde{z}/h = 0.50)$			
	−9.6803	−5.7876	−2.8319	−1.5943	−0.6491	−0.2955
			$\theta\,[\mathrm{K}]$ $(\tilde{z}/h = 0.50)$			
	0.1900	0.3597	0.4710	0.4924	0.4988	0.4997
			$\sigma_{\alpha\alpha}\,[10^{5}\,\mathrm{Pa}]$ $(\tilde{z}/h = 0.00)$			
	−1.2251	0.1658	2.1128	3.0566	3.5376	3.6597
			$\sigma_{\alpha\beta}\,[10^{3}\,\mathrm{Pa}]$ $(\tilde{z}/h = 0.50)$			
	−6.9889	−6.0177	9.1881	9.9831	5.4625	2.9753
			$\sigma_{zz}\,[10^{3}\,\mathrm{Pa}]$ $(\tilde{z}/h = 0.50)$			
	47.834	13.375	7.5826	5.5353	2.6962	1.4216
			$D_z\,[10^{-6}\,\mathrm{C/m^2}]$ $(\tilde{z}/h = 1.00)$			
	87.335	32.795	7.2280	2.4477	0.8243	0.3526

Table 17
B4. Three-layered *PZT-5A/Cadmium Selenide/PZT-5A* simply-supported spherical shell considering Load Boundary conditions LB2 ($\mathtt{D}_{z_t} = 0.1\,\mathrm{C/m^2}$, $\mathtt{D}_{z_b} = 0\,\mathrm{C/m^2}$ and $\Theta_t = 1\,\mathrm{K}$, $\Theta_b = 0\,\mathrm{K}$). Thickness coordinate $\tilde{z}$ goes from 0 to h. Tabular results are in terms of the maximum amplitudes at the specific and appropriate points of the $\alpha - \beta$ plane.

a/h	2	4	10	20	50	100
			$v\,[10^{-3}\,\mathrm{m}]$ $(\tilde{z}/h = 0.00)$			
	0.1618	−0.3765	−3.2097	−7.1485	−15.635	−28.454
			$w\,[10^{-3}\,\mathrm{m}]$ $(\tilde{z}/h = 0.00)$			
	0.4338	0.0656	−6.0742	−17.918	−44.558	−83.519
			$\phi\,[10^{6}\,\mathrm{V}]$ $(\tilde{z}/h = 0.00)$			
	−0.0608	−0.8856	−10.743	−46.051	−168.70	−361.23
			$\theta\,[10^{-2}\,\mathrm{K}]$ $(\tilde{z}/h = 0.50)$			
	0.1900	0.3597	0.4710	0.4924	0.4988	0.4997
			$\sigma_{\beta\beta}\,[10^{7}\,\mathrm{Pa}]$ $(\tilde{z}/h = 1.00)$			
	0.1111	−1.4476	−6.1600	−10.018	−12.178	−12.502
			$\sigma_{\alpha z}\,[10^{6}\,\mathrm{Pa}]$ $(\tilde{z}/h = 0.50)$			
	−4.7212	−7.8199	−8.4893	−5.2705	−1.8638	−0.8177
			$\sigma_{zz}\,[10^{6}\,\mathrm{Pa}]$ $(\tilde{z}/h = 0.50)$			
	1.5771	1.8059	2.4539	1.6679	0.6785	0.3258
			$D_z\,[10^{-3}\,\mathrm{C/m^2}]$ $(\tilde{z}/h = 0.50)$			
	0.9291	3.4354	15.490	32.192	46.232	49.169

CRediT authorship contribution statement

S. Brischetto: Writing – review & editing, Supervision, Software, Methodology, Conceptualization. **D. Cesare:** Writing – original draft, Visualization, Validation, Software, Investigation, Formal analysis, Data curation. **T. Mondino:** Visualization, Investigation, Formal analysis, Data curation.

Declaration of competing interest

The authors declare that they have no known competing financial interests or personal relationships that could have appeared to influence the work reported in this paper.

Data availability

Data will be made available on request.

References

[1] Varelis D, Saravanos DA. Coupled nonlinear mechanics for the electromechanical response of multi-stable piezoelectric shallow shells with piezoelectric films. Aerosp Sci Technol 2021;109(106444):1–18.

[2] Boccardi S, Ciampa F, Meo M. Design and development of a heatsink for thermo-electric power harvesting in aerospace applications. Smart Mater Struct 2019;28:1–18, 105057.

[3] Prasath S Sreenivasa, Arockiarajan A. Experimental and theoretical investigation on the thermo-electro-elastic properties of macro-fiber composites (MFC). Compos Struct 2015;122.

[4] Dehghan M, Nejad M Zamani, Moosaie A. Thermo-electro-elastic analysis of functionally graded piezoelectric shells of revolution: Governing equations and solutions for some simple cases. Internat J Engrg Sci 2016;104.

[5] Wu C-P, Chiu K-H, Wang Y-M. A review on the three-dimensional analytical approaches of multilayered and functionally graded piezoelectric plates and shells. CMC - Comput Mater Contin 2008;8(2):93–132.

[6] Arshid E, Soleimani-Javid Z, Amir S, Duc N Dinh. Higher-order hygro-magneto-electro-thermomechanical analysis of FG-GNPs-reinforced composite cylindrical shells embedded in PEM layers. Aerosp Sci Technol 2022;126(107573):1–19.

[7] Alibeigloo A. Coupled thermoelasticity analysis of FGM plate integrated with piezoelectric layers under thermal shock. J Therm Stresses 2019;42(11):1357–75.

[8] Dai HL, Wang X. Thermo-electro-elastic transient responses in piezoelectric hollow structures. Int J Solids Struct 2005;42:1151–71.

[9] Dube GP, Kapuria S, Dumir PC. Exact piezothermoelastic solution of simply-supported orthotropic flat panel in cylindrical bending. Int J Mech Sci 1996;38(11):1161–77.

[10] Georgiades AV, Challagulla KS, Kalamkarov AL. Modeling of the thermopiezoelastic behavior of prismatic smart composite structures made of orthotropic materials. Compos: Part B 2006;37(11):569–82.

[11] Kapuria S, Dumir PC, Sengupta S. An exact axisymmetric solution for a simply supported piezoelectric cylindrical shell. Archive Appl Mech 1997;67:260–73.

[12] Kapuria S, Dumir PC, Sengupta S. Three-dimensional solution for a hybrid cylindrical shell under axisymmetric thermoelectric load. Archive Appl Mech 1997;67:320–30.
[13] G. M Kulikov, Plotnikova SV. Exact 3D thermoelectroelastic analysis of piezoelectric plates through a sampling surfaces method. Mech Adv Mater Struct 2015;22:33–43.
[14] Kulikov GM, Plotnikova SV. Coupled thermoelectroelastic stress analysis of piezoelectric shells. Compos Struct 2015;124:65–76.
[15] Podil'chuk YN. Exact analytical solutions of static electroelastic and thermoelectroelastic problems for a transversely istropic doubly in curvilinear coordinate systems. Internat Appl Mech 2003;39(2):132–70.
[16] Quan T Quoc, Quyen N Van, Duc N Dinh. An analytical approach for nonlinear thermo-electro-elastic forced vibration of piezoelectric penta-graphene plates. Eur J Mech A Solids 2021;85(104095):1–13.
[17] Tang YY, Noor AK, Xu K. Assessment of computational models for thermoelectroelastic multilayered plates. Comput Struct 1996;61(5):915–33.
[18] Tauchert TR. Plane piezothermoelastic response of a hybrid laminate - a benchmark problem. Compos Struct 1997;39(3–4):329–36.
[19] Xu K, Noor AK, Tang YY. Three-dimensional solutions for coupled thermoelectroelastic response of multilayered plates. Comput Methods Appl Mech Engrg 1995;126:355–71.
[20] Zhang C, Cheung YK, Di S, Zhang N. The exact solution of coupled thermoelectroelastic behavior of piezoelectric laminates. Comput Structures 2002;80:1201–12.
[21] Zhang C, Di S, Zhang N. A new procedure for static analysis of thermo-electric laminated composite plates under cylindrical bending. Composite Structures 2002;56:131–40.
[22] Ninh D Gia, Tien N Duc. Investigation for electro-thermo-mechanical vibration of nanocomposite cylindrical shells with an internal fluid flow. Aerosp Sci Technol 2019;92:501–19.
[23] Zhao X, Iegaink FJN, Zhu WD, Li YH. Coupled thermo-electro-elastic forced vibrations of piezoelectric laminated beams by means of Green's functions. Int J Mech Sci 2019;156:355–69.
[24] Ahmad SN, Upadhyay CS, Venkatesan C. Electro-thermo-elastic formulation for the analysis of smart structures. Smart Materials Structures 2006;15:401–16.
[25] Baiz O, Benaissa H, Moutawakil D El, Fakhar R. Variational and numerical analysis of a static thermo-electro-elastic problem with friction. Math Probl Eng 2018;1–16, 8346891.
[26] Chen Q, Tu W, Liu R, Chen X. Parametric multiphysics finite-volume theory for periodic composites with thermo-electro-elastic phases. J Intell Mater Syst Struct 2018;29(4):530–52.
[27] Cho M, Oh J. Higher order zig-zag theory for fully coupled thermo-electric–mechanical smart composite plates. Int J Solids Struct 2004;41:1331–56.
[28] Jiang JP, Li DX. Finite element formulations for thermopiezoelastic laminated composite plates. Smart Mater Struct 2008;17:1–13.
[29] Li XY, Wang T, Zheng RF, Kang GZ. Fundamental thermo-electro-elastic solutions for 1D hexagonal QC. ZAMM - Z Für Angew Math Und Mech 2015;95(5):457–68.
[30] Li P, Li X, Wang T. Three-dimensional thermo-electro-elastic field in a circular plate of functional graded materials with transverse isotropy. Mech Adv Materials Structures 2015;22:537–47.
[31] Liew KM, Zhang JZ, Li C, Meguid SA. Three-dimensional analysis of the coupled thermo-piezoelectro-mechanical behaviour of multilayered plates using the differential quadrature technique. Int J Solids Struct 2005;42:4239–57.
[32] Long Y, Yu W. Asymptotical modeling of thermopiezoelastic laminates. Smart Mater Struct 2016;25:1–13, 015002.
[33] Moradi-Dastjerdi R, Behdinan K. Thermo-electro-mechanical behavior of an advanced smart lightweight sandwich plate. Aerosp Sci Technol 2020;106:106142.
[34] Tornabene F, Viscoti M, Dimitri R. Effect of thermal and electric coupling on the multifield response of laminated shell structures employing higher-order theories. Compos Struct 2025;354:1–36, 118801.
[35] Wang X, Chen Y, Yu J, Liu Y, Zhang B, Zhou H. Reflection, transmission, and dissipation of plane waves in sandwiched functionally graded thermo-electro-elastic nanoplates via nonlocal integral elasticity theory. Compos Struct 2023;324:1–16, 117564.
[36] Wu C-P, Chiu K-H, Jiang R-Y. A meshless collocation method for the coupled analysis of functionally graded piezo-thermo-elastic shells and plates under thermal loads. Internat J Engrg Sci 2012;56:29–48.
[37] Yu W, Hodges DH. A simple thermopiezoelastic model for smart composite plates with accurate stress recovery. Smart Mater Struct 2004;13:926–38.
[38] Yu W, Hodges DH. Mathematical construction of an engineering thermopiezoelastic model for smart composite shells. Smart Mater Struct 2005;14:43–55.
[39] Zenkour AM, Alghanmi RA. Static response of sandwich plates with FG core and piezoelectric faces under thermo-electro-mechanical loads and resting on elastic foundations. Thin-Walled Struct 2020;157(107025):1–14.
[40] Brischetto S. Exact three-dimensional static analysis of single- and multi-layered plates and shells. Compos Part B 2017;119:230–52.
[41] Brischetto S, Cesare D. 3D electro-elastic static analysis of advanced plates and shells. Int J Mech Sci 2024;280:1–29, 109620.
[42] Brischetto S, Cesare D. Three dimensional coupling between elastic and thermal fields in the static analysis of multilayered composite shells. CMES - Comput Model Eng Sci 2023;136(3):2551–94.
[43] Hildebrand FB, Reissner E, Thomas GB. Notes on the foundations of the theory of small displacements of orthotropic shells. 1949, NACA - National Advisory Committee for Aeronautics, Technical Note No. 1833, Washington (U.S.A.).
[44] Brischetto S, Cesare D. Three-dimensional vibration analysis of multilayered composite and functionally graded piezoelectric plates and shells. Compos Struct 2024;346:1–24, 118413.
[45] Povstenko Y. Fractional thermoelasticity. Switzerland: Springer International Publishing; 2015.
[46] Brischetto S, Torre R. Convergence investigation for the exponential matrix and mathematical layers in the static analysis of multilayered composite structures. J Compos Sci 2017;1(2):1–15, 19.
[47] Brischetto S, Carrera E. Coupled thermo-mechanical analysis of one-layered and multilayered isotropic and composite shells. CMES - Comput Model Eng Sci 2010;56(3):249–301.
[48] Chen C-Q, Shen Y-P, Wang X-M. Exact solution of orthotropic cylindrical shell with piezoelectric layers under cylindrical bending. Int J Solids Struct 1996;33(30):4481–94.